Nonlinear dynamic analysis of three-dimensional bladed-disks with frictional contact interfaces based on cyclic reduction strategies

Samuel Quaegebeur, Benjamin Chouvion, Fabrice Thouverez

Nonlinear dynamic analysis of three-dimensional bladed-disks with frictional contact interfaces based on cyclic reduction strategies

Samuel Quaegebeur[a,b,*], Benjamin Chouvion[c], Fabrice Thouverez[b]

[a] *Safran Helicopter Engines, 64511 Bordes, France*
[b] *Ecole Centrale de Lyon, LTDS UMR 5513, 69130 Ecully, France*
[c] *Centre de recherche de l'Ecole de l'air, 13661 Salon-de-Provence, France*

Abstract

In bladed disks, friction nonlinearities occurring within the contact between the blades and disk or between the blades and underplatform dampers are used to decrease the vibratory energy of the system and extend its lifespan. Modeling these nonlinearities and simulating their effects correctly are challenging: complex nonlinear phenomena such as stick, slip and separation may occur in the contact zones. Efficient numerical methods must be used to compute the dynamics of the system in a reasonable amount of time. This paper proposes a new reduction methodology to tackle large cyclically symmetric finite-element models undergoing static preload from centrifugal effects and strong nonlinearities (friction and separation). It combines the nonlinear identification of the possible interacting nodal diameters with a linear component mode synthesis procedure. Its performances are assessed through comparisons with some state-of-the art methods. Complex and realistic nonlinear finite-element models of bladed disks with underplatform dampers and dovetail or fir-tree blade roots are used. The Dynamic Lagrangian Frequency Time algorithm is employed to capture the nonlinear effects. Using the proposed new reduction methodology, the effect of underplatform dampers on bladed disk contact occurrence and damping efficiency is investigated.

*Corresponding author
Email address: samuel.quaegebeur@ec-lyon.fr (Samuel Quaegebeur)

Keywords: Cyclic symmetry, Friction nonlinearities, Traveling and standing wave excitations, Harmonic Balance Method, Underplatform damper

1. Introduction

Vibration is widely present in turbomachinery. Engineers seek to decrease its level in order to extend engine lifespan and reduce the cost of maintenance. Introducing friction nonlinearities, such as contact between blades and disk or blades and underplatform dampers, is widely used as a damping mechanism. This paper will focus on these two different nonlinearities, considered either separately or combined together.

Different designs of friction dampers have been studied by Petrov [1, 2]. The work of Gola et al. [3] underlined the complex behavior of underplatform dampers. Yang and Menq [4] proposed an approach to design wedge dampers. Sanliturk et al. [5] and Pesaresi et al. [6, 7] provided experimental validation of their models. Many parametric simulations have been run to study the contact parameter [8] or the effect of centrifugal loading [9] on system dynamics. Firrone et al. [10, 11], and more recently Pesaresi et al. [6], underscored the importance of considering both the centrifugal effect and the external force within the nonlinear solver for an accurate response.

For efficient simulation of the dynamics of nonlinear structures composed of blades, disk and contact regions, three successive methodologies must be chosen: one to characterize the nonlinear effects occurring at the contact zones, one to reduce the size of the model usually constructed by finite elements and, finally, one to diminish the number of evaluations of the nonlinear forces. Numerous methodologies have been proposed to describe the contact at frictional interfaces accurately. Zucca et al. [12] proposed strategies to model friction nonlinearities for 1D and 2D contact. Nacivet et al. [13] developed the Dynamic Lagrangian Frequency Time (DLFT) algorithm which employs Coulomb's law along with a Harmonic Balance Method (HBM) [14] and an Alternating Frequency Time

(AFT) [15] procedure. Mitra et al. [16] proposed a nonlinear reduced-order model (ROM) by using a basis formed by multiple levels of sticking and slipping cases.

The entire structural model under consideration is composed of nonlinear degrees of freedom (DOFs) at interfaces and linear ones everywhere else. To decrease the computational time, it is interesting to reduce the number of linear DOFs. Different strategies have been developed over the years for this purpose. Classical component mode synthesis methods (CMS) [17] are widely employed in industry. Petrov [18] proposed an approach to reduce the evaluation of the dynamic stiffness matrix. Mashayekhi et al. [19] employed a similar approach for mistuned structures. Pourkiaee and Zucca [20] also provided reduction strategies specific to the case of shrouded blade models. For cyclic symmetric systems, some of the aforementioned reduction methods can be employed in addition to the cyclic symmetric procedure [21, 22] which enables a drastic reduction in the numerical system to be solved. However, in the presence of nonlinearities, the nodal diameters get coupled [23] and the system may remain large.

This paper focuses on a nonlinear, perfectly cyclic, bladed disk structure modeled with a high number of finite elements. The most direct approach to account for the nonlinear effects would be to evaluate all the nonlinear forces for all sectors. This exact approach, which is necessary for mistuned structures [19], requires a very long computation time. However, other methods have been developed in the case of perfectly cyclic structures. Petrov [24] proposed a reduction methodology based on the assumption that both the deformation and external forcing show the same wave shape. This work has then been widely used to study different effects due to, for instance, underplatform dampers [1] or fretting wear of the bladed disk [25]. However, this strategy is efficient only when the external force has a traveling wave shape. In a recent paper [26], we proposed a theoretical method to predict which nodal diameters get coupled in the presence of friction nonlinearities, leading to a much-reduced nonlinear system. This work was merely validated on

a phenomenological model of a bladed disk, in which centrifugal load and loss of contact between solids were not studied. Another possible approach is the Component Nonlinear Complex Mode Synthesis (CNCMS) method, proposed by Joannin et al. [27, 28], which employs CMS reduction but also deals with the nonlinear evaluation by considering complex nonlinear modes calculated on a fixed-boundary sector.

In this paper, a new cyclic reduction method to tackle large nonlinear finite element models undergoing centrifugal load is developed. This strategy combines a linear component mode synthesis procedure [17] with a nonlinear nodal diameter reduction [26]. Several options were given in [26] to select the important nodal diameters. These options will all be considered in the new methodology. The proposed reduction method is employed and validated on a cyclic structure with dovetail attachment (the contact is described by frictional effects at interfaces but also by possible separation). Such level of validation is very scarce in the literature, even for a well-known method such as [24]. The authors intend, through this paper, to promote this new method as a possible reference methodology to assess the accuracy of new reduced-order models.

The different nonlinear methodologies used in this paper will be presented briefly in Section 2. Section 3 will compare their efficiency and accuracy when applied to a simplified bladed disk finite-element model. Finally, Section 4 provides some useful insights into the influence of underplatform dampers on the dynamics of a realistic bladed disk model.

2. Methodologies

This section presents the different reduction methodologies that will be employed later to study bladed disks composed of multiple solids: a disk, N blades, and possibly N dampers, as illustrated in Figure 1 in the case of a structure with $N = 8$ sectors and no dampers.

2.1. Linear reduction

When the structure is modeled with finite elements, we usually begin by reducing the linear part of the system with classical CMS [17] methods. In this paper, the Craig-Bampton procedure is employed [29]. The structure is broken down into master degrees of freedom (DOFs) $\mathbf{u}_\mathrm{m}$ and slave DOFs $\mathbf{u}_\mathrm{s}$. $\mathbf{u}_\mathrm{s}$ is reduced into n_ξ generalized coordinates, noted $\boldsymbol{\xi}$ with the equation:

$$\begin{bmatrix} \mathbf{u}_\mathrm{m} \\ \mathbf{u}_\mathrm{s} \end{bmatrix} = \mathbf{R} \begin{bmatrix} \mathbf{u}_\mathrm{m} \\ \boldsymbol{\xi} \end{bmatrix} = \begin{bmatrix} \mathbf{I} & \mathbf{0} \\ \boldsymbol{\Psi} & \boldsymbol{\Phi} \end{bmatrix} \begin{bmatrix} \mathbf{u}_\mathrm{m} \\ \boldsymbol{\xi} \end{bmatrix} \tag{1}$$

where $\mathbf{R}$ is the reduction matrix and is composed of linear static mode shapes $\boldsymbol{\Psi}$ (obtained with a unit displacement for each master DOF), and linear modes $\boldsymbol{\Phi}$ obtained for $\mathbf{u}_m = 0$. The matrix $\mathbf{I}$ is the identity matrix. The static mode shapes and linear modes are obtained respectively by

$$\boldsymbol{\Psi} = -\mathbf{K}_{\mathrm{f,ss}}^{-1}\mathbf{K}_{\mathrm{f,sm}}, \tag{2}$$

$$\left(-\omega^2\mathbf{M}_{\mathrm{f,ss}} + \mathbf{K}_{\mathrm{f,ss}}\right)\boldsymbol{\Phi} = \mathbf{0}. \tag{3}$$

where $\mathbf{M}_{\mathrm{f},ss}$, $\mathbf{K}_{\mathrm{f},ss}$ and so on denote partitions (slave-slave DOFs) of the full mass and stiffness matrices $\mathbf{M}_\mathrm{f}$ and $\mathbf{K}_\mathrm{f}$. As illustrated with red lines in Figure 1, the nonlinear regions can be located in the contact zone between the blades and the disk, for instance. In these regions, different nonlinear phenomena may occur: stick, slip and/or separation [30]. To compute the nonlinear dynamics of the system, these DOFs must be kept as master DOFs, as well as (at least) one observer node on which the external excitation will be applied. This standard reduction is widely used in the paper and is employed in the different methodologies explained hereafter, whose accuracy will be studied in Section 3.

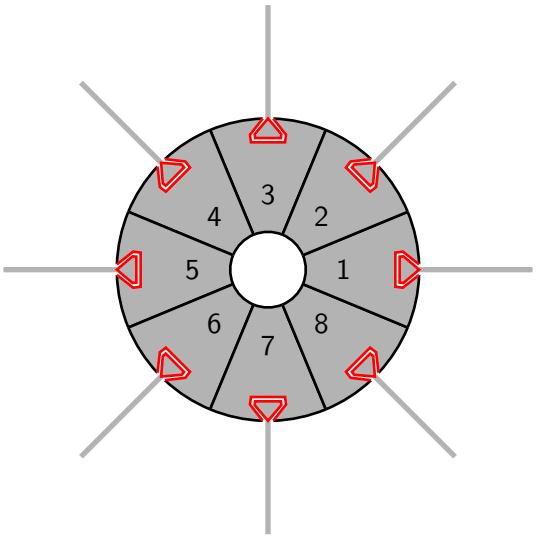

Figure 1: Cyclic symmetric structure with $N = 8$ and nonlinear contact occurring at the blade root.

2.2. Reference method

A rotational speed Ω was first applied to the different components, leading, among other things, to a static preload that is retrieved from the ANSYS commercial FE software. Applying the Craig-Bampton procedure to the full finite-element model results in the following nonlinear system:

$$\mathbf{M}\ddot{\mathbf{u}} + \mathbf{C}\dot{\mathbf{u}} + \mathbf{K}\mathbf{u} + \mathbf{f}_{\text{nl}} = \mathbf{f}_{\text{ext}}, \tag{4}$$

where $\mathbf{M}$ and $\mathbf{K}$ are the mass and stiffness matrices obtained from the reduction procedure. The damping matrix $\mathbf{C}$ will be constructed in order to obtain a modal damping of 5×10^{-4} for the mode studied. The vector $\mathbf{f}_{\text{ext}}$ contains both the static preload and dynamic external excitation force; $\mathbf{f}_{\text{nl}}$ denotes the nonlinear forces. As in [11, 6], the static and dynamic loadings are coupled in the work presented in this paper. The external excitation force in turboengines may follow a specific wave pattern because a given stage can be excited either by previous stages due to the incoming air, or by a forward stage due to reverse airflow.

If the stages alternate between a rotating bladed disk and a fixed one, the excitation force follows a traveling wave shape. This force $\mathbf{f}_{\text{ext,j}}$, for a sector j, can be described with the following equation

$$\mathbf{f}_{j,\text{ext}} = \mathbf{f}_{1,\text{ext}}\left(t - \frac{2\pi h_{ex}\,(j-1)}{\omega N}\right), \tag{5}$$

where N denotes the number of sectors, h_{ex} is the excitation wave number and ω is the relative speed between two stages. In other situations, the bladed disk may be excited by a standing wave force which is then defined as the combination of waves traveling in the opposite direction:

$$\mathbf{f}_{j,\text{ext}} = \frac{1}{2}\left(\mathbf{f}_{1,\text{ext}}\left(t - \frac{2\pi h_{ex}\,(j-1)}{\omega N}\right) + \mathbf{f}_{1,\text{ext}}\left(t + \frac{2\pi h_{ex}\,(j-1)}{\omega N}\right)\right). \tag{6}$$

2.3. Component Nonlinear Complex Mode Synthesis (CNCMS) method

Joannin et al. proposed a reduction approach called CNCMS to tackle both tuned and mistuned cyclic structures with friction nonlinearities. Their initial work [27] presented the methodology for a one-dimensional spring-masses model and was then extended for 3D finite-element models in [28]. In the latter paper, the CNCMS procedure was broken down into three steps: a classical Craig-Bampton reduction for each detuned sector (see Equation (1)), a nonlinear Craig-Bampton procedure to recover the complex nonlinear modes of a sector [31] and finally the use of interface mode reduction [17]. The final superelement created was composed of $N \times N_{\text{mode}} + N_{\text{interf}}$ complex unknowns (one control coordinate per sector multiplied by the number of nonlinear modes N_{mode} considered supplemented by N_{interf} interface modes). It depended on the excitation frequency and was employed in a synthesis procedure to calculate the forced response. The nonlinear forces were synthesized from the nonlinear modes computed at the second reduction step [32]. The application of the CNCMS method in this paper will be slightly different in that we will use the static preload due to the global rotation, whereas a uniform static preload was

applied in [28]. The CNCMS will be compared with other methods in Section 3 to evaluate its accuracy and efficiency as a ROM methodology.

2.4. Cyclic symmetry methodologies

For tuned cyclic structures, the problem can be written in terms of spectral components, also called nodal diameters [33, 21, 22]. In a finite-element approach, combining this change of variables with a Craig-Bampton procedure enables the creation of $(K+1)$ superelements (one for each nodal diameter) directly from a single sector; where $K = \frac{N}{2}$ if N is even or $K = \frac{N-1}{2}$ otherwise. These superelements contain master DOFs composed of the nonlinear DOFs as well as an observer node. Compared to the reference method presented in Section 2.2, this strategy allows us to decrease the Craig-Bampton computation time drastically because the reduction is applied to a single sector only. Compared to the CNCMS procedure in Section 2.3, the cyclic property allows us to consider the cyclic boundary as slave DOFs. In this paper, we will assume that the cyclic boundaries are free of nonlinearities. For linear problems, the spectral formulation yields an uncoupled system of equations [34] and is extremely advantageous. However, in the presence of nonlinearities, the equation of motion couples the different nodal diameters and can be written as:

$$\tilde{\mathbf{M}}_k \ddot{\tilde{\mathbf{u}}}_k + \tilde{\mathbf{C}}_k \dot{\tilde{\mathbf{u}}}_k + \tilde{\mathbf{K}}_k \tilde{\mathbf{u}}_k + \mathbf{F}_k^T \mathbf{f}_{\text{nl}} = \tilde{\mathbf{f}}_{\text{ext},k}, \qquad \forall k \in [\![0, K]\!], \tag{7}$$

with $\tilde{\mathbf{M}}_k$, $\tilde{\mathbf{C}}_k$ and $\tilde{\mathbf{K}}_k$ the mass, damping and stiffness spectral matrices of order k. The vectors $\tilde{\mathbf{u}}_k$, and $\tilde{\mathbf{f}}_{\text{ext},k}$ denote the spectral displacement, nonlinear force and excitation force of order k. $\mathbf{F}_k^T$ denotes the Fourier transform associated with the $k-$th spectral component. If all spectral components are considered up to K, the number of coupled nonlinear unknowns of (7) is equal to the number of equations in (4) and thus no reduction is obtained. Moreover, the nonlinear forces must be evaluated for all sectors, a priori.

Different strategies, such as [24, 26], exist to decrease the size of (7) and reduce the number of sectors for which the nonlinear forces must be evaluated. In a general manner, after reduction the system becomes:

$$\tilde{\mathbf{M}}_k\ddot{\tilde{\mathbf{u}}}_k + \tilde{\mathbf{C}}_k\dot{\tilde{\mathbf{u}}}_k + \tilde{\mathbf{K}}_k\tilde{\mathbf{u}}_k + \mathbf{F}_k^T\mathbf{Q}\left(\mathbf{f}_{\mathrm{nl},m}\right) = \tilde{\mathbf{f}}_{\mathrm{ext},k}, \qquad k \in k_m \tag{8}$$

where $\mathbf{Q}$ is an operator which verifies

$$\mathbf{f}_{\mathrm{nl}} = \mathbf{Q}\left(\mathbf{f}_{\mathrm{nl},m}\right). \tag{9}$$

The operator $\mathbf{Q}$ allows the number of sectors for which the nonlinear forces must be evaluated to be reduced: only a subset of the nonlinear forces, noted $\mathbf{f}_{\mathrm{nl},m}$, is used to determine the nonlinear forces on all sectors. The space k_m gathers the nodal diameters which interact through the nonlinearities. The original approach of this paper is to combine the Craig-Bampton reduction, explained in Section 2.1, with the different options proposed in [26], referred to as Method 1 and Method 2 (the same terminology is employed in this paper). The method developed in [24] also uses cyclic symmetry property. All these cyclic methods define their own $\mathbf{Q}$ and k_m. These are detailed next.

Method 1. For Method 1 [26], the set k_m is determined analytically by considering friction nonlinearities. This method is highly robust as it is entirely theoretical and makes no assumptions. The evaluation of the nonlinear forces is performed with

$$\mathbf{Q}\left(\mathbf{f}_{\mathrm{nl},m}\right) = \mathbf{P}\mathbf{f}_{\mathrm{nl},m} \tag{10}$$

where the matrix $\mathbf{P}$ can be obtained by the real (Re) and imaginary (Im) parts of the Fourier matrix and is equal to

$$\mathbf{P} = \begin{bmatrix} \mathbf{I}_{N_{\mathrm{diam}}} & \\ \left[\mathrm{Re}\left(\mathbf{F}_2\right) \quad \mathrm{Im}\left(\mathbf{F}_2\right)\right] & \left[\mathrm{Re}\left(\mathbf{F}_1\right) \quad \mathrm{Im}\left(\mathbf{F}_1\right)\right]^{-1} \end{bmatrix}. \tag{11}$$

The terms $\mathbf{F}_1$ and $\mathbf{F}_2$ denote partitions of the Fourier matrix associated with the interacting nodal diameters. While $\mathbf{F}_1$ is the partition for the first N_{diam} sectors (equal to the number of interacting nodal diameters, weighted by 2 if $k \notin \{0, \frac{N}{2}\}$), $\mathbf{F}_2$ is the partition for the $N - N_{\text{diam}}$ sectors. Its full derivation is given in [26]. The term $\mathbf{f}_{\text{nl},m}$, in Equation (10), gathers the nonlinear forces of the first N_{diam} sectors.

Method of Petrov [24]. In [24], the set k_m is not known a priori (and is determined by the resolution method, which is detailed in Section 2.5). This methodology is applicable only if the structure is excited with a traveling wave excitation. It assumes that both the deformation of the structure and associated nonlinear force have a traveling wave shape. The operator $\mathbf{Q}$ must therefore ensure that for a sector $j \in [\![1, N]\!]$

$$\mathbf{f}_{\text{nl},j} = \mathbf{f}_{\text{nl},1}\left(t - \frac{2\pi h_{ex}(j-1)}{\omega N}\right). \tag{12}$$

Evaluating the nonlinear forces for a single sector is thus sufficient to compute the nonlinear frequency forced response of the entire structure. This offers greater reduction than Method 1, but only works for traveling wave excitation.

Method 2. Method 2 combines the analytical results of Method 1 (determination of the set k_m) but also uses the assumption of traveling wave excitation, displacement, and nonlinear forces ($\mathbf{Q}$ must ensure Equation (12)).

2.5. Numerical solution methods and contact algorithm

The nonlinear system obtained by the methodologies presented in Sections 2.2 to 2.4 can be solved with different methods. We can cite, for instance, numerical time integration, Asymptotic Numerical Methods (ANM) [35] or shooting methods [36]. In this paper, we will employ the Harmonic Balance Method [37, 38] which is explained next.

The HBM can be broken down into a projection step and an orthogonalization step. To solve the full nonlinear system (4), the projection stage seeks the solution as a Fourier series up to an order N_h,

$$\mathbf{u}(t) = \frac{1}{2}\left(\mathbf{c}_0 + \sum_{n=1}^{N_h} \mathbf{c}_n e^{ni\omega t}\right) + c.c, \tag{13}$$

where the coefficients $(\mathbf{c}_n)_{n\in[\![0,N_h]\!]}$ are the harmonics coefficients. The excitation frequency is noted by ω. The terms $c.c$ represent the complex conjugate terms. The orthogonalization step projects the system obtained after substituting the displacement $\mathbf{u}$ written as in (13) into (4). The projection is made on the exponential basis $\left(e^{ni\omega t}\right)_{n\in[\![0,N_h]\!]}$. Finally, we obtain from (4) the system

$$\mathbf{Z}_n\mathbf{c}_n + \mathbf{c}_{\mathbf{f}_{\text{nl}},n} = \mathbf{c}_{\mathbf{f}_{\text{ext}},n}, \qquad \forall n \in [\![0,N_h]\!], \tag{14}$$

where $\mathbf{Z}_n = (ni\omega)^2\mathbf{M} + (ni\omega)\mathbf{C} + \mathbf{K}$ is the dynamic stiffness matrix associated with the harmonic n. The terms $\mathbf{c}_{\mathbf{f}_{\text{nl}},n}$, respectively $\mathbf{c}_{\mathbf{f}_{\text{ext}},n}$, represent the projection of the nonlinear force, respectively the excitation force, on the exponential basis. In this paper, the excitation is supposed to be mono-harmonic, hence $\mathbf{c}_{\mathbf{f}_{\text{ext}},n} \neq 0$ for $n = 1$ only. In the following, we give further explanations on how the HBM is applied in the different cyclic reduction methodologies.

Method 1. Method 1 explained in Section 2.4 considers only the interacting nodal diameters ($k \in k_m$). To solve (8), the projection step of the HBM seeks the solutions as

$$\begin{aligned} \tilde{\mathbf{u}}_k &= \sum_{n=-N_h}^{N_h} \tilde{\mathbf{c}}_{k,n} e^{ni\omega t} && \text{for } k \notin \left\{0, \tfrac{N}{2}\right\} \\ \tilde{\mathbf{u}}_k &= \frac{1}{2}\left(\sum_{n=0}^{N_h} \tilde{\mathbf{c}}_{k,n} e^{ni\omega t}\right) + c.c && \text{for } k \in \left\{0, \tfrac{N}{2}\right\}. \end{aligned} \tag{15}$$

For $k = 0$ and $k = \dfrac{N}{2}$ (if N is even), the spectral component is a real quantity, whereas it is a complex value for other $k-$ values.

Method of Petrov [24]. Assuming a traveling wave shape (Equation (12)) with the HBM expansion (Equation (13)) allows the harmonics number n to be paired with specific spectral component $\tilde{\mathbf{u}}_k$. For each spectral component $\tilde{\mathbf{u}}_k$, its associated set of harmonics is noted $\mathscr{N}_k$ and is sought as,

$$\begin{aligned} \tilde{\mathbf{u}}_k &= \sum_{n\in\mathscr{N}_k} \tilde{\mathbf{c}}_{k,n} e^{ni\omega t} && \text{for } k \notin \left\{0, \tfrac{N}{2}\right\} \\ \tilde{\mathbf{u}}_k &= \frac{1}{2}\left(\sum_{n\in\mathscr{N}_k} \tilde{\mathbf{c}}_{k,n} e^{ni\omega t}\right) + c.c && \text{for } k \in \left\{0, \tfrac{N}{2}\right\}. \end{aligned} \tag{16}$$

By determining the non-zero values of the spectral components in Equation (16), we can then determine the set k_m in Equation (8).

Method 2. The displacement obtained from Method 2 follows Equation (16). However only the interacting nodal diameters obtained from [26] are considered, and hence some harmonics are not retained in the expansion.

All these methods can be employed with different contact methodologies. In this paper, we use a Schur condensation [39], which allows the different systems of equations to be reduced to their relative nonlinear DOFs. The nonlinear forces are calculated using these relative DOFs and with the Dynamic Lagrangian Frequency Time algorithm [13]. This procedure assumes no regularization of the friction law and also handles the existence of possible separation between the two bodies in the contact region. The contact/separation between the body satisfies the following law:

$$\begin{cases} \mathbf{f}_{\mathrm{nl},N}(t) \geq 0 & \text{repulsive force only} \\ \mathbf{x}_{r,N}(t) \geq 0 & \text{no penetration} \\ \mathbf{x}_{r,N}(t) \cdot \mathbf{f}_{\mathrm{nl},N}(t) = 0 & \text{either no force or no contact} \end{cases}, \tag{17}$$

where the subscript N denotes the normal direction of the contact and $\mathbf{x}_r$ represents the relative displacement between the solids on the contact area. If the bodies are in contact,

then frictional effects are modeled using Coulomb's law,

$$\begin{cases} \|\mathbf{f}_{\mathrm{nl},T}\| < \mu \left|\mathbf{f}_{\mathrm{nl},N}\right| & \text{if } \dot{\mathbf{x}}_{r,T} = 0 \\ \mathbf{f}_{\mathrm{nl},T} = -\mu \left|\mathbf{f}_{\mathrm{nl},N}\right| \dfrac{\dot{\mathbf{x}}_{r,T}}{\|\dot{\mathbf{x}}_{r,T}\|} & \text{if } \|\dot{\mathbf{x}}_{r,T}\| > 0, \end{cases} \tag{18}$$

where the subscript T denotes the tangential directions. Appendix A details the numerical implementation of the DLFT.

2.6. Summary of the strategies

To summarize the different approaches, this section presents the various stages of reduction, as well as the size of the final system. The features of the different methods are summarized in Table 1. $N_{\mathrm{dof,nl}}$ represents the relative number of nonlinear DOFs for one sector. For Method 1, the number N_{diam} is equal to the number of interacting nodal diameters (with a factor 2 in the case $k \notin \left\{0, \frac{N}{2}\right\}$). Table 2 provides N_{diam} for different values of external excitations (combined with the static preload $h_{ex} = 0$) and with $N = 24$.

The pairing employed in [24] is used for Method 2, but the harmonics which do not excite a specific interacting nodal diameter are removed. Therefore the number of harmonics is reduced to $N_{h,2}$ in Method 2. For the CNCMS, the complex nonlinear mode is evaluated with the HBM with N_h harmonics; however, the synthesis stage is only performed with the first harmonic.

Methodologies	Reduction stages	Number of unknowns	Type of excitation
Reference method	1st: Craig Bampton	$N \times N_{\text{dof,nl}} \times (1+2N_h)$	Any
CNCMS	1st: Craig Bampton 2nd: Nonlinear Craig Bampton 3rd: Interfaces Modes	$(N \times N_{\text{mode}} + N_{\text{interf}}) \times 2$	Any
Petrov's method [24]	1st: Cyclic symmetry 2nd: Craig Bampton 3rd: Selection of the nodal diameter	$N_{\text{dof,nl}} \times (1+2N_h)$	Traveling
Method 1	1st: Cyclic symmetry 2nd: Craig Bampton 3rd: Selection of the nodal diameter	$N_{\text{diam}} \times N_{\text{dof,nl}} \times (1+2N_h)$	Any
Method 2	1st: Cyclic symmetry 2nd: Craig Bampton 3rd: Selection of the nodal diameter	$N_{\text{dof,nl}} \times \left(1+2N_{h,2}\right)$	Traveling

Table 1: Specificities of the different methodologies.

The reduction offered by Method 1 is not as efficient as that with Petrov's method or Method 2, but it is exact for friction nonlinearities and can be employed for any excitation. Although the CNCMS requires additional reduction stages and is thus more complicated to implement, its performances seem interesting. It is also valid for any kind of excitations.

Moreover, except for the CNCMS, these methods can be employed with other reductions, such as [18], rather than CMS methods. The objective of the next section is to provide information on the accuracy of the different methodologies.

$\mathbf{h_{ex}}$	0	1	2	3	4	5	6	7	8	9	10	11	12
$\mathbf{N_{diam}}$	1	13	7	5	4	13	3	13	3	5	7	13	2

Table 2: Number of interacting diameters N_{diam} for 24 sectors (see Appendix A in [26]).

3. Performance and accuracy of the methodologies

The different methodologies presented in Section 2 are benchmarked on a finite-element model with a variable number of blades. The discretization used in these models makes it possible to apply the reference method of the system presented in Section 2.2. A variable number of blades is used to increase the modal density of the cyclic system and also to increase the amount of nonlinear effect transmitted through the cyclic boundaries. This study will give insights into the possible limitations of the different methods.

3.1. Presentation of the simplified test case

The model studied is composed of a 100 mm diameter disk and N blades (each of length 60 mm) with typical dovetail attachments. It was used in [25] to study fretting wear. The number of blades varies between $\{6, 12, 18, 24\}$. Each contact interface is discretized with 15 nodes (3×5). With 3 DOFs per node, and 2 contact interfaces, each of these models contains 180 nonlinear DOFs, all situated at the blade/disk interfaces. Figure 2a represents the model with $N = 24$ blades. The full sector (see Figure 2b) is composed of 25920 DOFs. The nonlinear interfaces are illustrated as green surfaces in Figures 2c and 2d. A rotational speed of $\Omega = 1000\,\text{rad}\,\text{s}^{-1}$ was applied on the system leading to a static preload. The gyroscopic effect was assumed negligible and not taken into account

in the analysis. The inner region of the disk was clamped. An 0.32N excitation force was applied at the tip of the blade with either a traveling or a standing wave shape (see Equations (5) and (6)). The associated wave number was varied arbitrarily and is given in the numerical results. The nonlinear forces were evaluated with the DLFT algorithm with a friction coefficient of $\mu = 0.3$. The HBM procedure was employed with $N_h = 3$ (which is a good compromise choice between accuracy and computation time, and is commonly used, for instance in [6]), and with the constant harmonic term (corresponding to $\mathbf{c}_0$ or $\tilde{\mathbf{c}}_{0,n}$ in Equations (13), (15) or (16)).

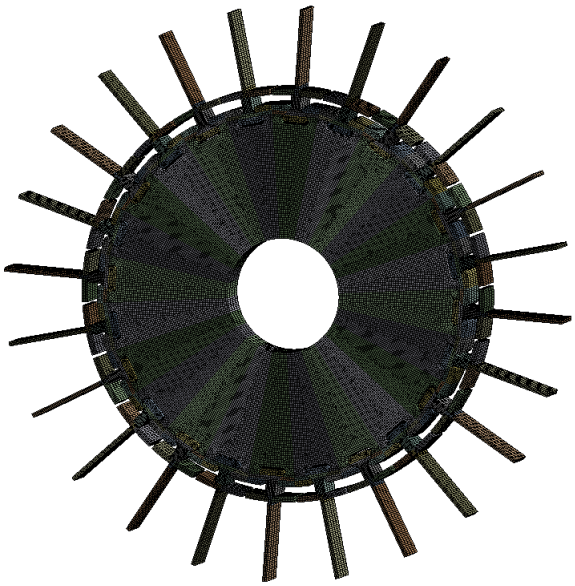

(a) Description of the full finite-element model with 24 sectors.

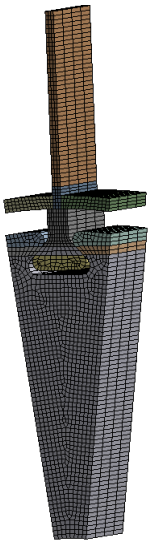

(b) Fundamental sector.

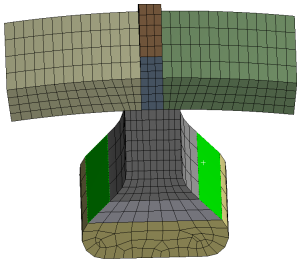

(c) Blade nonlinear region.

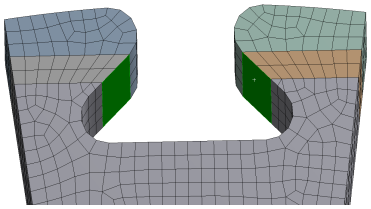

(d) Disk nonlinear region.

Figure 2: Structural mesh of the bladed disk model.

3.2. Linear analysis

A linear numerical simulation was first performed with the ANSYS commercial FE software for the test case $N = 24$ and an excitation on the third nodal diameter ($h_{ex} = 3$). Figure 3a represents the amplitude of the tip of the blade in the frequency range of the first three modes of the system.

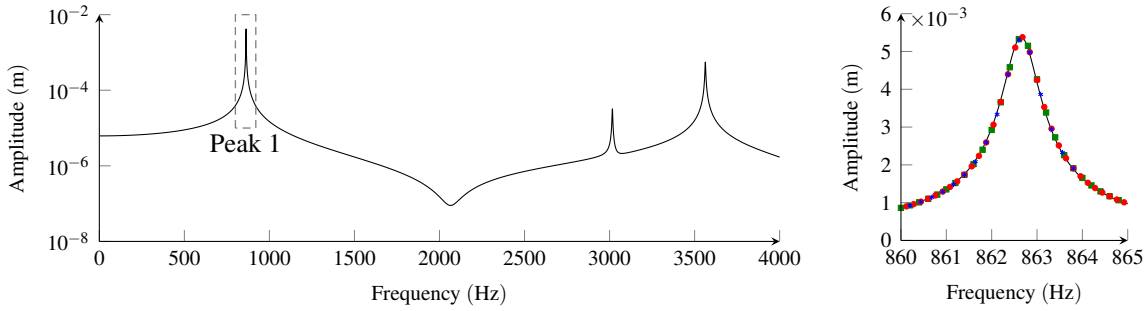

(a) ANSYS linear (stuck response).

(b) Peak 1.

Figure 3: Linear response (—): ANSYS; (■): reference method; (●): Cyclic methods; (✱): CNCMS.

The first peak corresponds to the first flapwise flexural mode, the second is a combination between torsion and an edge flexion, and the third mode is the first torsion mode. In all the following simulations, the first flexural mode of the system, situated around 860 Hz, is studied. Each method employed a Craig-Bampton reduction with a sufficiently high number of modes, such that the dynamics of this mode were captured accurately, see Figure 3b. The CNCMS method was run with the first linear mode and 300 interface modes and also gives accurate prediction on the first flexural mode.

To capture the second and third linear peaks correctly, all three methodologies need a greater number of Craig-Bampton modes. However, note that the CNCMS would also need the computation of more linear modes, as well as additional interface modes.

3.3. Nonlinear numerical results

The following results present the amplitude at the tip of the blade for the different sectors under harmonic forcing around the first linear flexural natural frequency.

3.3.1. Traveling wave excitation

A traveling wave excitation was first applied to the system. Figure 4 illustrates the results obtained with the reference method, the CNCMS approach (run with the first non-

linear mode and 300 interfaces modes), Petrov's methodology, Method 1 and Method 2 for different numbers of blades and excitation wave numbers. All the sectors show the same frequency forced response, hence only a single curve per method is represented in Figure 4.

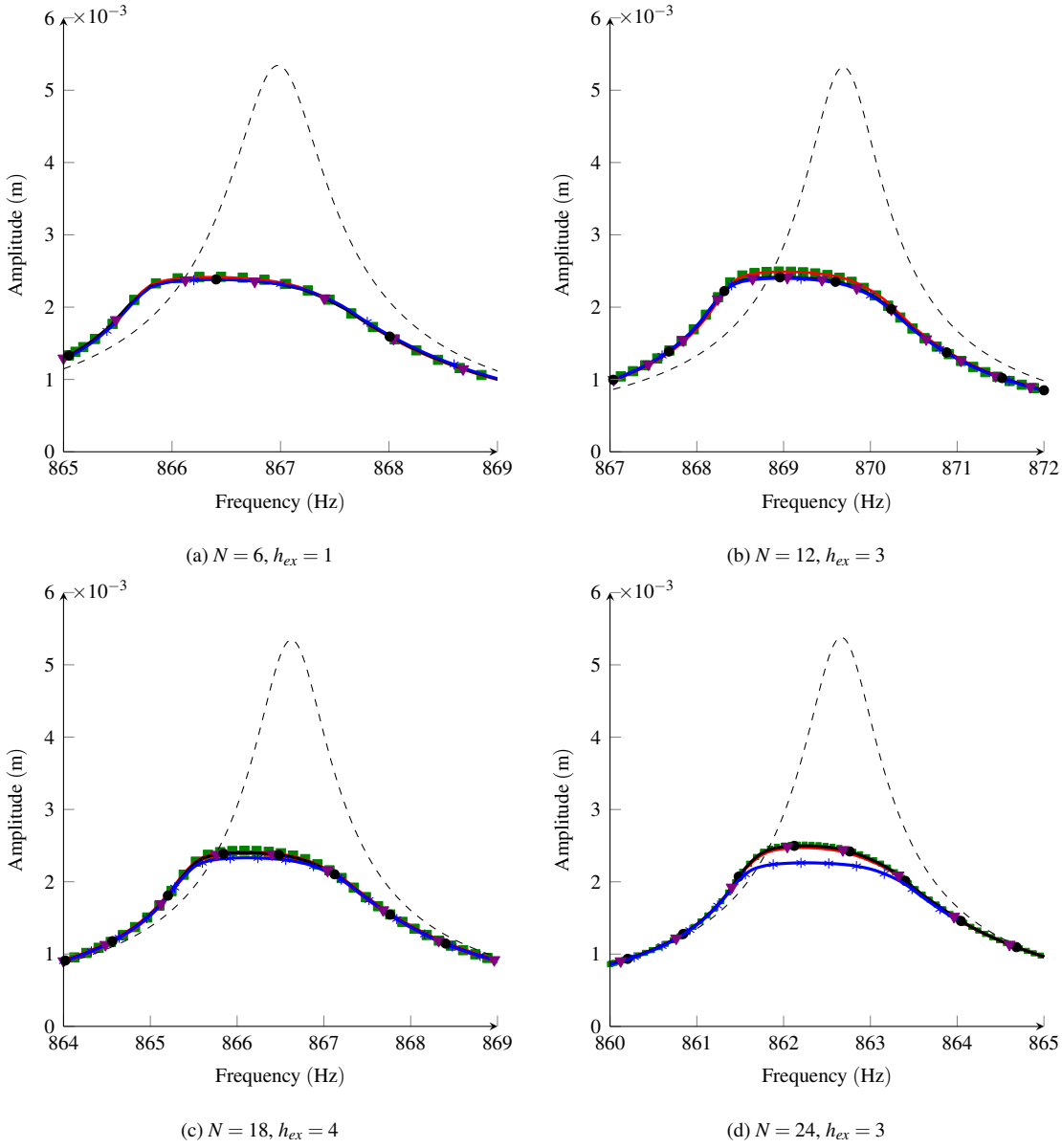

(a) $N = 6$, $h_{ex} = 1$

(b) $N = 12$, $h_{ex} = 3$

(c) $N = 18$, $h_{ex} = 4$

(d) $N = 24$, $h_{ex} = 3$

Figure 4: Frequency forced response under a traveling wave excitation for different numbers of sectors and excitation wave numbers. (- -): linear solution (fully stuck); (■): reference solution; (-+-): CNCMS; (▼): Petrov's method; (-●-): Method 1; (—): Method 2.

322 Figure 4 shows a similar behavior regardless of the number of sectors: due to friction

and separation of nodes at the different interface regions, the nonlinear amplitude is approximately half that of the linear response. The higher the number of sectors, the larger the error becomes between the CNCMS procedure and the reference solution. This observation is highlighted in Table 3 in which the maximum relative errors are given. The maximum error was calculated with

$$\text{error} = \max_{j} \left(\max_{\omega} \left(\left| \frac{u_{\text{ref},j} - u_{\text{RM},j}}{u_{\text{ref},j}} \right| \right) \right), \tag{19}$$

where $u_{\text{ref},j}$ and $u_{\text{RM},j}$ denote respectively the reference solution and the reduction methodology solution for a sector j. The inaccuracy of the CNCMS is due to the second stage of reduction: the nonlinear Craig-Bampton. This step evaluates the nonlinear mode with fixed boundaries and corrects this approximation by linear static mode shapes. For a high number of sectors (the cyclic boundaries are close to the nonlinear regions) and a high level of nonlinearity, the linear static mode shapes cannot transmit the nonlinear contributions correctly to the neighbouring sectors.

Number of sectors	6	12	18	24
CNCMS	1.7%	3.6%	4.1%	10.4%
Petrov's method	1.4%	3.2%	1.2%	0.6%
Method 1	1.4%	3.2%	1.2%	0.6%
Method 2	0.2%	0.1%	1.2%	1.6%

Table 3: Relative error in the case of a traveling wave excitation.

For Method 1, Method 2 and Petrov's method, the responses are very accurate. A small discrepancy may be observed in Figure 4b for Petrov's method (which corresponds to the 3.2% error in Table 3). This result is rather surprising, especially with the corresponding 0.1% error of Method 2. For this specific test case, both methodologies take into account

both the nodal diameter 0 (with the 0^{th} harmonic) and nodal diameter 3 (with the 1^{st} and 3^{rd} harmonics). Petrov's method also considers nodal diameter 6 with the 2^{nd} harmonic. Therefore this additional unknown, which at first sight proposes more flexibility in the solution, creates a small error. It can be assumed that this result is specific to this test case in which the different assumptions may somehow offset one another.

3.3.2. Standing wave excitation

A standing wave excitation was now applied to the structure. Figure 5 presents the results obtained with the reference method, the CNCMS approach, and Method 1 (both Petrov's method and Method 2 are inappropriate with a standing wave excitation). Contrary to the traveling wave case, the sectors present different levels of amplitude.

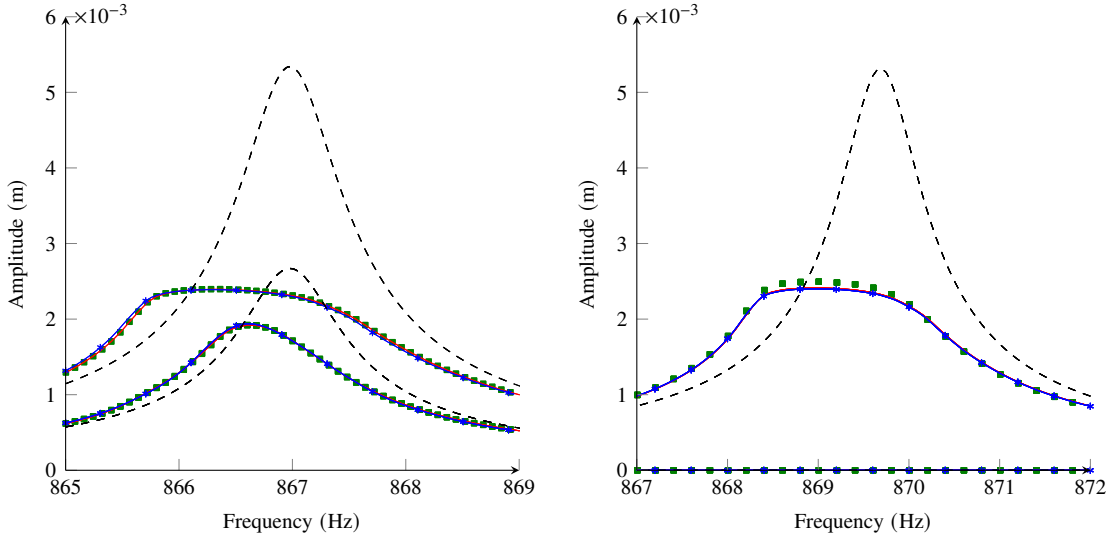

(a) $N = 6$, $h_{ex} = 1$.

(b) For $N = 12$, $h_{ex} = 3$.

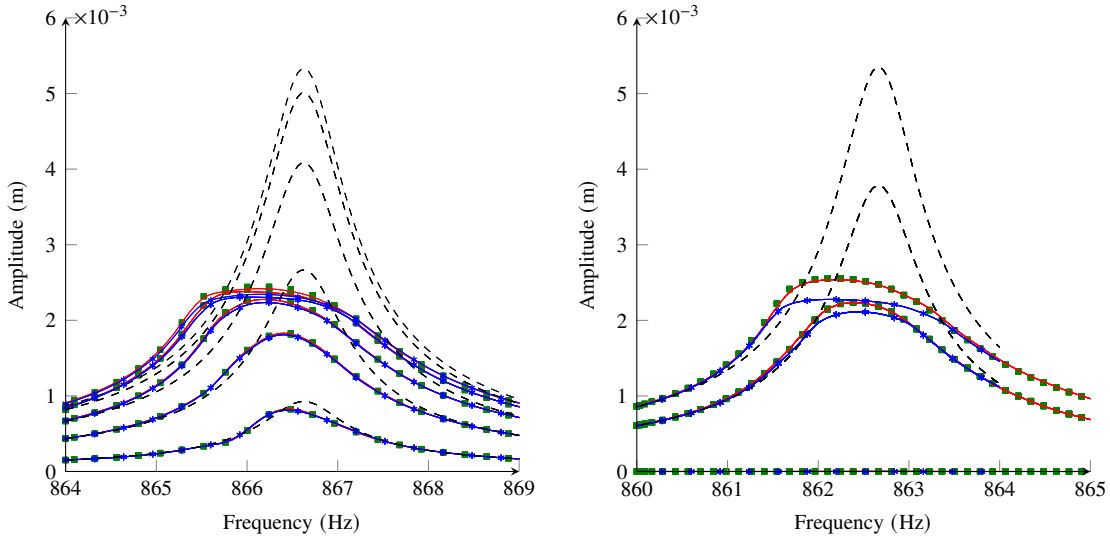

(c) $N = 18$, $h_{ex} = 4$.

(d) $N = 24$, $h_{ex} = 3$.

Figure 5: Frequency forced response under a standing wave excitation for different numbers of sectors and excitation wave numbers. (- -): linear solution (fully stuck); (■): reference solution; (-✱-): CNCMS; (—): Method 1.

349 The amplitude responses and overall behavior of Figure 5 is quite different to those

shown in Figure 4 due to the different excitation. As will be explained in more detail in Section 3.4, the way the energy is exchanged within the system between the nodal diameters is different in the case of a traveling or a standing wave excitation. Similarly to Figure 4, we observe that the relative error of the CNCMS gets higher as the number of sectors increases. As depicted in Table 4, Method 1 is very accurate. The maximum level of error reached for $N = 12$ (3.2%) is explained next.

Number of sectors	6	12	18	24
CNCMS	2.5%	3.6%	4.1%	10.9%
Method 1	1.6%	3.2%	1.1%	0.6%

Table 4: Relative error for standing wave excitation.

Method 1 does not make any assumption on the shape of the solution. It is based on an analytical development of nodal diameter interactions in the presence of friction non-linearities. However, as the DLFT algorithm used in the simulations manages to capture states of separation, the nodes may be in one of the three following states over a period: totally separated (there is no contact, therefore Method 1 is exact), never separated (once again Method 1 is exact as the nodes may be stuck or sliding), or undergoing a partial separation (alternating between contact and separation over one period). For this last case, Method 1 is not exact and may be inaccurate.

In order to provide a global view of the contact status of the nodes at the interface, Figure 6 presents the average status of all nodes over the period (discretized into n_{it} instants) for Method 1 (illustrated using lines) and the reference method (depicted with square and circle markers). The full lines (or squares) represent the percentage of nodes undergoing separation (colored green), stick (colored red) and slip (colored blue) behavior. For

example, in the case of separation, this percentage is calculated with

$$\%\text{separation} = \frac{1}{n_{it}} \sum_{it=1}^{n_{it}} \left(\frac{1}{N_{\text{dof,nl}}} \sum_{\text{node}=1}^{N_{\text{dof,nl}}} (\text{contact}\,(it, \text{node}) == \text{separation}) \right) \times 100, \quad (20)$$

with $\text{contact}\,(it, \text{node}) == \text{separation}$ equal to 1 if the contact of the node is separated at time it, and 0 otherwise. Moreover, in Figure 6, the dotted lines (or circles) denote the percentage of nodes undergoing a constant status over the entire period. The same color code is used to represent this status. For the constant separation case for instance, it is calculated with

$$\%\text{separation}_{\text{tot}} = \frac{1}{N_{\text{dof,nl}}} \sum_{\text{node}=1}^{N_{\text{dof,nl}}} (\text{contact}\,(\forall it, \text{node}) == \text{separation}) \times 100, \quad (21)$$

with $\text{contact}\,(\forall it, \text{node}) == \text{separation}$ equal to 1 if the contact node is separated at all times and 0 otherwise. The average percentage of stuck or sliding nodes is calculated in a way similar to Equations (20) and (21). This post-treatment enables the overall contact status of the system to be described. As an example, Figure 6c shows at 864 Hz that the nodes are mostly stuck (98% overall and about 50% are stuck at all time). Method 1 provides results close to the reference solution (small discrepancies are obtained for $N = 12$ and $N = 24$ but the overall trend is respected).

Furthermore this post-treatment enables the level of accuracy of Method 1 to be quantified reasonably: if partial separation occurs (presented by a difference between the full green line and the dotted green line in Figure 6) then it explains why Method 1 is no longer exact. For instance, for $N = 6$, 12, 18 and 24 sectors the nodes undergo respectively partial separation at a maximum level of 6%, 8%, 1% and 0.2% (note that the dotted green lines are equal to 0 for all numbers of sectors and hence no node is fully separated). A direct

correlation can then be made with Table 4: the error level increases with the percentage of partial separation.

A similar analysis cannot be made to explain differences obtained with Method 2 in Section 3.3.1. This method makes the additional assumption of a traveling wave shape solution: the error obtained can therefore be due to a combination of different assumptions.

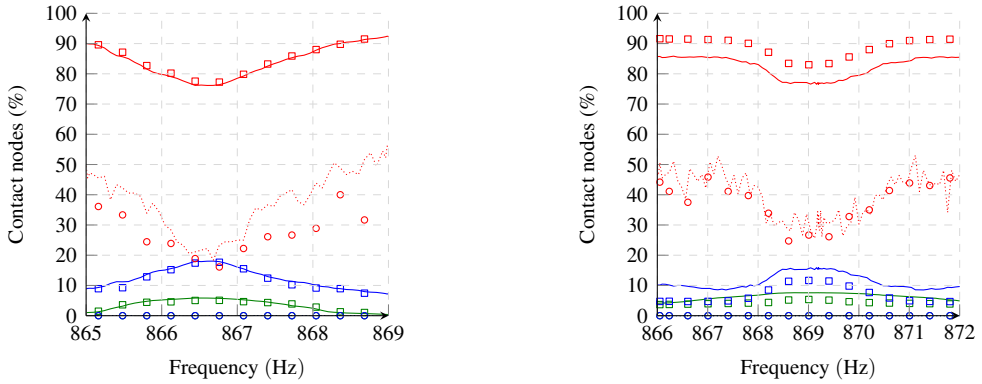

(a) $N = 6$, $h_{ex} = 1$.

(b) $N = 12$ and $h_{ex} = 3$.

(c) $N = 18$ and $h_{ex} = 4$.

(d) $N = 24$ and $h_{ex} = 3$.

Figure 6: Average contact status of the nodes over a period. (—): separation; (—): stuck; (—): slip calculated with Method 1. For each contact status, (·····) with the same color code corresponds to the percentage of which the status does not change over time. (□), respectively (○), shows the results associated with (—), respectively (·····), but obtained with the reference solution (the same color code is used).

3.4. Details on the spectral contents of the responses for the $N = 24$ case

While Figure 4d (obtained with a traveling wave excitation) showed a single level of amplitude for all sectors, Figure 5d (obtained with a standing wave excitation) shows different levels. To better highlight why such differences occur, we now focus on the spectral content of the different responses. As demonstrated in [26], the friction nonlinearities create coupling between the zeroth, third and ninth nodal diameters (the external excitation follows a wave pattern with $h_{ex} = 3$ and the static preload corresponds to a 0 diameter excitation). Those are the diameters illustrated in Figure 7. The reference solution also contains a negligible amplitude response (below 1×10^{-7} m) on other nodal diameters due to separation and these diameters are therefore not represented.

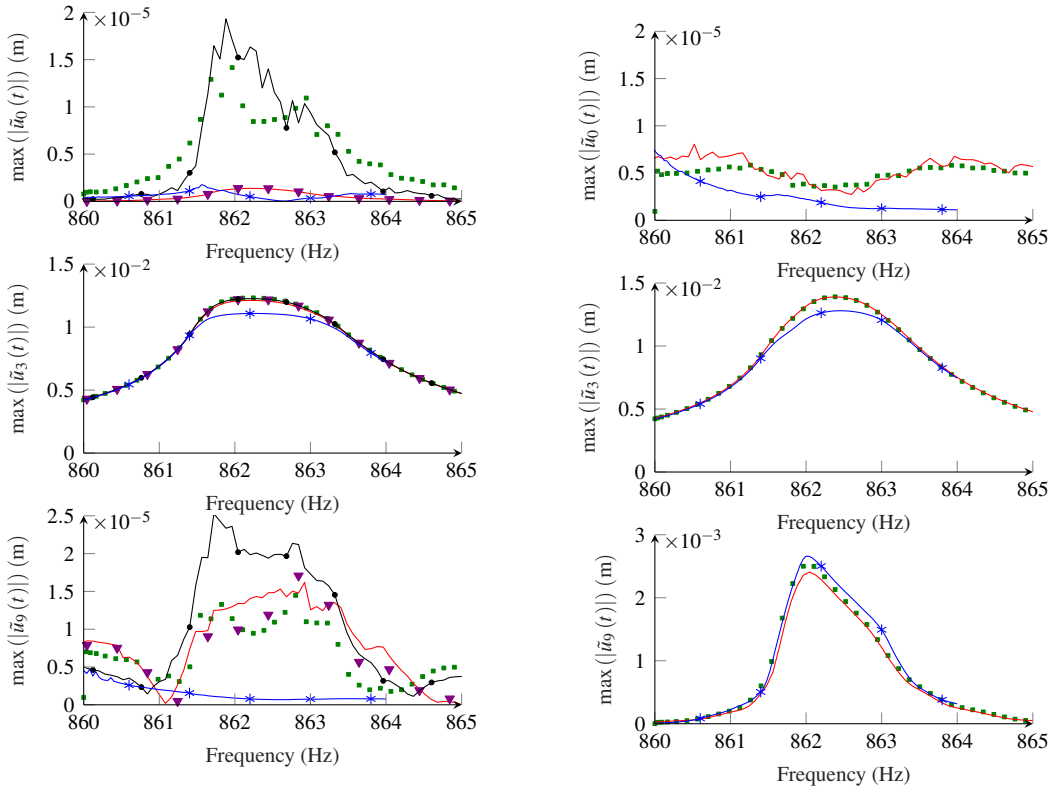

(a) Traveling wave excitation. (■): reference solution; (-✱-): CNCMS; (▼): Petrov's method; (-●-): Method 1; (—): Method 2.

(b) Standing wave excitation. (■): reference solution; (-✱-): CNCMS; (—): Method 1.

Figure 7: spectral contents of the responses illustrated in Figure 4d and 5d

In the case of a traveling wave excitation, the different methods capture the trend of $\tilde{u}_3$ correctly (except for the 10% error of the CNCMS) and give a correct order of magnitude for $\tilde{u}_9$. However for $\tilde{u}_0$, the different methodologies (except Method 1) capture neither the correct trend nor the order of magnitude.

Some details on the harmonics composition of these spectral components are provided in Figure 8 at a specific frequency. Both Petrov's method and Method 2 assume a traveling wave displacement which manages to capture the harmonic -1 of $\tilde{u}_3$ correctly and thus the overall behavior of the system. However, the harmonic content of the reference

411 solution clearly shows that the solution is not a pure traveling wave solution (as an exam-
412 ple, $\tilde{u}_9$ responds on the harmonics -1 and 1 with an amplitude greater than the harmonic
413 -3). Overall, Method 1 manages to capture most of the harmonics correctly. Some dis-
414 crepancies can be observed, however these discrepancies are for low values of harmonics
415 amplitudes and do not impact the amplitude of structural vibration (as underlined in Ta-
416 ble 3).

417 In the case of a standing wave excitation, Method 1 manages to capture the dynamics
418 of $\tilde{u}_0$, $\tilde{u}_3$ and $\tilde{u}_9$ correctly, as observed in Figure 7b. The harmonics content, shown in
419 Figure 8b, clearly exhibits a standing wave solution (because $\tilde{c}_{k,n} = \bar{\tilde{c}}_{k,-n}$).

420 From Figure 8a and 8b, we observe that the coupling between the third and ninth nodal
421 diameters is 1000 times greater for a standing wave than for a traveling wave. Therefore it
422 seems that nodal diameter interactions is facilitated when the structure is under a standing
423 wave excitation.

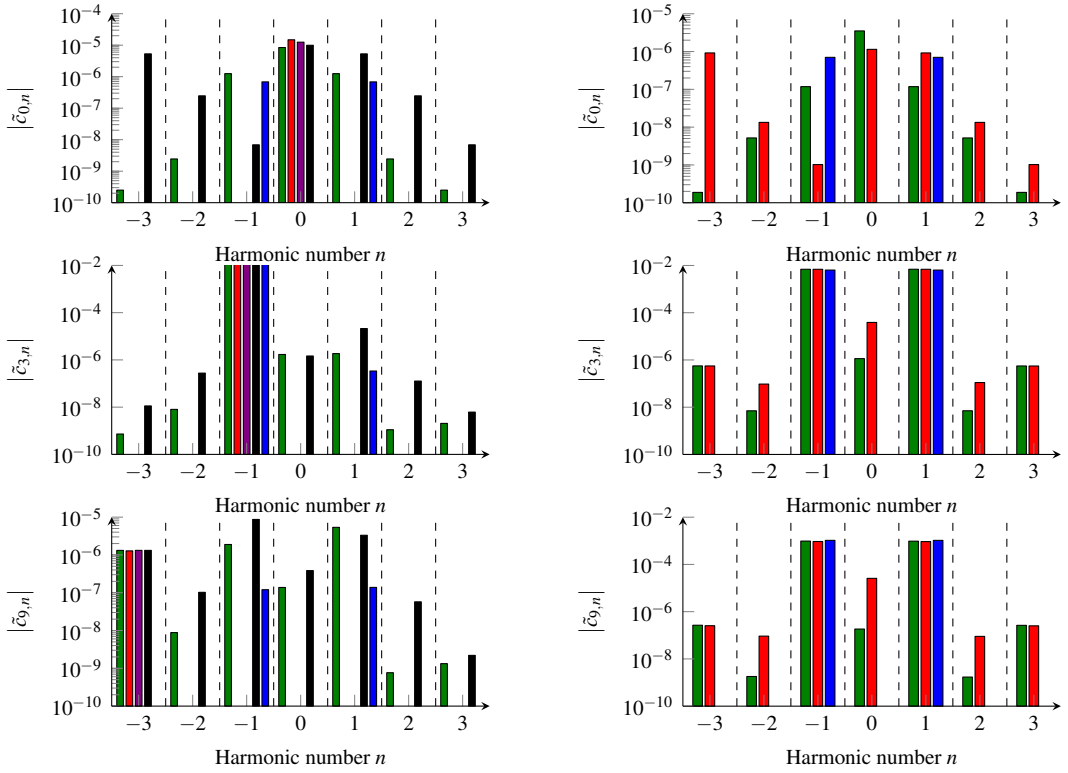

(a) Traveling wave excitation (the color code matches the one of Figure 7a).

(b) Standing wave excitation (the color code matches the one of Figure 7b).

Figure 8: Harmonics contents of the responses given in Figure 7a and 7b calculated at 862.4 Hz.

3.5. *Performance of the methods*

Tables 5 and 6 set out approximated computation times obtained with the different methodologies applied to the system with 24 sectors[1]. Only the computation time of the frequency forced response is provided. The preprocessing time is not included in Tables 5 and 6. The CNCMS method first required the evaluation of a nonlinear mode which took 27 min. However this mode has been computed only once and can be used for any excitation.

[1]The simulations were run on an Intel(R) Core(TM) i7-7700 @ 3.6 GHz computer

Method	Number of unknowns	Computation time
HBM full system	15120	5 h
CNCMS	648	12 min
Petrov's Method [24]	630	40 s
Method 1	3150	17 min
Method 2	450	24 s

Table 5: Performance of the methods in the case of a traveling wave excitation (with 24 sectors).

Method	Number of unknowns	Computation time
HBM full system	15120	6 h
CNCMS	648	13 min
Method 1	3150	18 min

Table 6: Performance of the methods in the case of a standing wave excitation (with 24 sectors).

In the case of a traveling wave excitation, Petrov's method and Method 2 are highly efficient: the computation time is greatly reduced compared to the reference method or the CNCMS method. Method 1 requires a longer computation time but offers more flexibility as it can handle any kind of excitation. The CNCMS approach also reduces the computation time but shows some inaccuracy for a high level of nonlinearity and a high number of sectors. However the capacity of the CNCMS to handle mistuning [34] makes it interesting with a low level of nonlinearity. Studying the effect of mistuning is beyond the scope of the current paper.

4. Damping mechanisms for a bladed disk with underplatform dampers

Section 3 showed that Method 1 and Method 2 are accurate and efficient as reduction models to tackle nonlinear finite-element models. Using these, we investigate in this section the influence of underplatforms dampers for a bladed disk with fir-tree attachment. These parameter studies could have not been performed without the existence and validation of such high-standard reduction methods.

4.1. Presentation of the test case

The finite-element model considered is shown in Figure 9 and is a realistic representation of a compressor stage. Multiple nonlinear regions exist: the bladed disk fir-tree attachment (see Figure 9c where the nonlinear interfaces are in green) and the underplatform dampers (see Figure 9d). The full sector is composed of 30840 DOFs (14430 for the blade, 14628 for the disk and 1782 for the underplatform dampers). Quadratic elements were employed for the analysis. The bladed disk contact is described with 432 nonlinear DOFs and the contact blade/dampers with 306 nonlinear DOFs. A rotational speed of $\Omega = 2200\,\mathrm{rad\,s^{-1}}$ is initially applied on the system. A $4 \times 10^{-1}\,\mathrm{N}$ excitation force is applied at the tip of the blade with either a traveling or a standing wave shape (see Equations (5) and (6)) with $h_{ex} = 3$. Three configurations were studied: a bladed disk with no dampers (the nonlinear contact occurs only between the blades and the disk, see Figure 10a), a stuck bladed disk with dampers (the nonlinear contact occurs only between the dampers and the blades, see Figure 10b), and finally a full structure with blade, disk and dampers (nonlinear contact occurs between the blades, the disk and the dampers, see Figure 10c). The nonlinear forces were evaluated with the DLFT algorithm with a friction coefficient of $\mu = 0.15$. The HBM procedure is employed with $N_h = 3$.

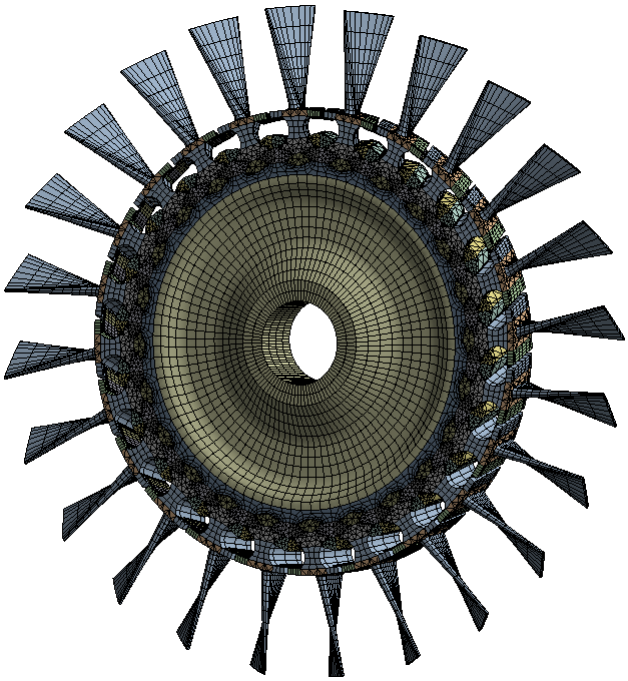

(a) Full structure.

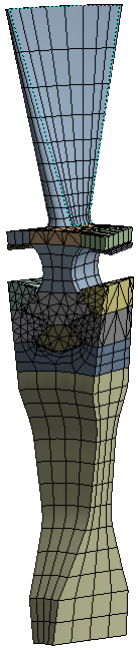

(b) Fundamental sector.

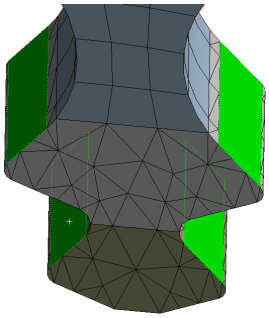

(c) Fir-tree attachment.

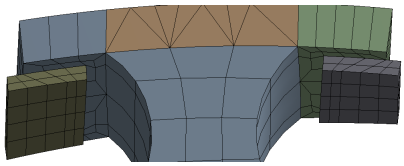

(d) Underplatform dampers.

Figure 9: Details on the realistic finite-element bladed disk.

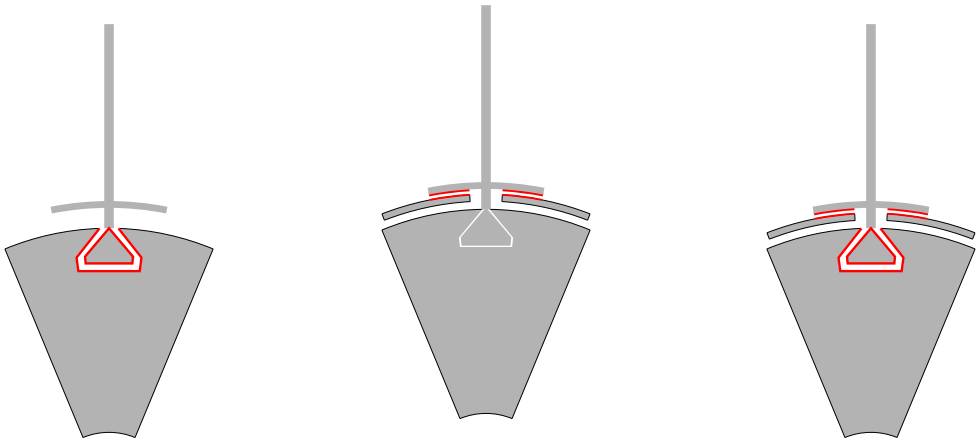

(a) Test case 1: bladed disk.

(b) Test case 2: stuck bladed disk with dampers.

(c) Test case 3: full nonlinear system.

Figure 10: Illustration of the test cases considered. The nonlinear frictional interfaces accounted for are depicted in red.

4.2. Numerical results on the standard test case

In the following, as in Section 3, two kinds of excitations were considered: a traveling excitation and a standing excitation. As the reference solution presented in Section 2.2 is no longer computable on a standard computer due to the number of nonlinear DOFs, we will then use respectively Method 2 and Method 1 to simulate the nonlinear dynamics of the structure. In order to get full confidence in the results obtained with Method 2, we also performed the same simulations with Petrov's method. The harmonics content of each nodal diameter for the different methods are provided in Table 7. The excitation frequency was varied around the natural frequency of the 1^{st} flexural mode. Once again, the frequency forced responses illustrated represent the displacement at the tip of the blades for all sectors.

Nodal diameters	Petrov's method [24]	Method 2	Method 1
0	0	0	$[\![0,3]\!]$
3	1	1	$[\![0,3]\!]$
6	2	n/a	n/a
9	3	3	$[\![0,3]\!]$

Table 7: Harmonics content of the spectral displacements for the different methodologies.

4.2.1. Traveling wave excitation

Figure 11 presents the frequency forced response of the three systems mentioned previously and illustrated in Figure 10. For the linear cases (stuck systems), represented by black dashed lines in Figure 11, we observe that the presence of dampers shifts the linear frequency towards high frequencies: the peak is reached at either 1538 Hz (Figure 11a without dampers) or 1586 Hz (Figure 11b and 11c with dampers). This result can simply be explained by the fact that the dampers add rigidity to the system. For the nonlinear bladed disk system, Figure 11a shows results similar to those presented in Section 3: the peak is damped by approximately 35% and is shifted to the low frequencies when the nonlinear effects are accounted for (friction and separation). For the stuck bladed disk with dampers, the results of which are illustrated in Figure 11b, the effects due to the nonlinearities are magnified: a shift of 8 Hz is observed and the damping is increased up to 55%. As Figure 11c (corresponding to the full system) is similar to Figure 11b, we can conclude that the nonlinear effects are mainly governed by the dampers and not by the blade root attachment.

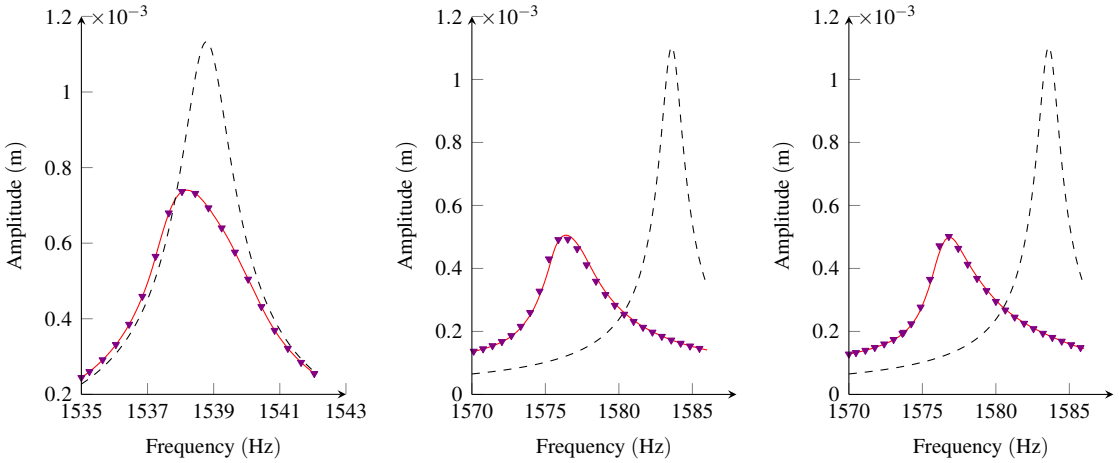

(a) Bladed disk. (b) Stuck bladed disk with dampers (c) Bladed disk with dampers.

Figure 11: Frequency forced response under a traveling wave excitation. (- -): linear solution (fully stuck); (▾): Petrov's method; (—): Method 2.

Figure 12 depicts the overall contact behavior of the three nonlinear systems whose forced response, calculated with Method 2, is illustrated in Figure 11. To better highlight how the nonlinear regions in the full system (blade/disk and blade/dampers) interact with each other, the contact status for each region is illustrated separately in Figure 12c. Doing so facilitates the comparison between Figure 12c and Figure 12a to study the bladed disk contact and between Figure 12c and Figure 12b to study the blade/damper contact.

For the bladed disk (see Figure 12a), 5% of the nodes are totally separated. Moreover, as only 2% (difference between the solid and dotted green lines) of the nodes undergo partial separation, the results are expected to be accurate (see Section 3.3.2). The dynamics are completely different in the case of a stuck bladed disk with dampers (see Figure 12b) where 50% of the nodes are separated. At the resonant peak, more nodes undergo partial separation (the difference between the solid and dotted green lines is approximately 10%) and there are more nodes in the slipping phase than in the stuck phase (the blue line moves above the red line in Figure 12b). Figure 12c describes the contact in the case of the

full nonlinear system. Overall, the behaviors match between Figure 12c, Figure 12a, and Figure 12b. However, we do observe in Figure 12c that approximately 90% of the blade nodes are stuck, whereas there is a decrease to 80% in Figure 12a. This expresses the fact that the energy of the system is mainly lost in the dampers and thus the vibration in the fir-tree attachment is reduced. Overall, we see that damper nonlinearity is of the upmost importance to capture the global dynamics of the system, as well as the loss of vibratory energy.

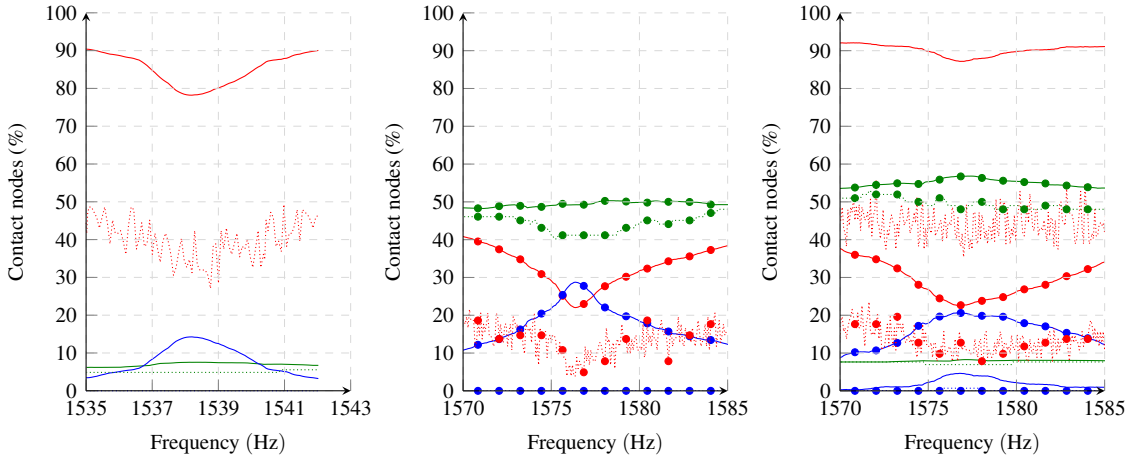

(a) Bladed disk. (b) Stuck bladed disk with dampers. (c) Bladed disk with dampers.

Figure 12: Average contact status of the nodes over a period, in the case of a traveling wave excitation, and with $\mu = 0.15$. (—): separation; (—): stuck; (—): slip for the blades/disk contact. (-●-) with the same color code corresponds to damper/blades contact. For each contact status, (·····) and (·●·), with the same color code, correspond to the percentage of which the status does not change over time.

4.2.2. Standing wave excitation

A standing wave excitation was now applied to the different test cases and the associated frequency forced responses calculated with Method 1 are given in Figure 13. For the three test cases, the amplitude of the tip of the blade on the first sector is globally the same for both types of excitation (comparison between Figures 11 and 13).

The contact status of the three configurations over the same frequency range is provided in Figure 14 and exhibits differences with the case of a traveling wave excitation. First, we observe that approximately 10% of the nodes are slipping in Figure 14a against 15% in Figure 12a. This indicates that the traveling wave excitation facilitates the appearance of friction. This can easily be explained by the fact that for a traveling wave solution, all the sectors undergo the same movement as that presented in Figure 11a. However, for a standing wave solution, some sectors get a very small amount of energy and remain stuck. This effect is accentuated for the stuck bladed disk with dampers, where 15% of the nodes are slipping under a standing wave excitation (see Figure 14b) against 30% for the traveling wave excitation (see Figure 12b).

Another difference between the traveling and standing wave excitations is the number of separated nodes in the full nonlinear test case. Whereas the separation effect was largely dominant (approximately 55%) for the damper/blade contact in the case of a traveling wave excitation (see Figure 12c), the stuck phase predominates in the case of a standing wave excitation (see Figure 14c). As this observation was not made for the stuck bladed disk with dampers case (Figure 14b), we can expect this effect to come from the coupling between the standing wave excitation creating different levels of energy for the sectors and the nonlinearity between the blades and disk.

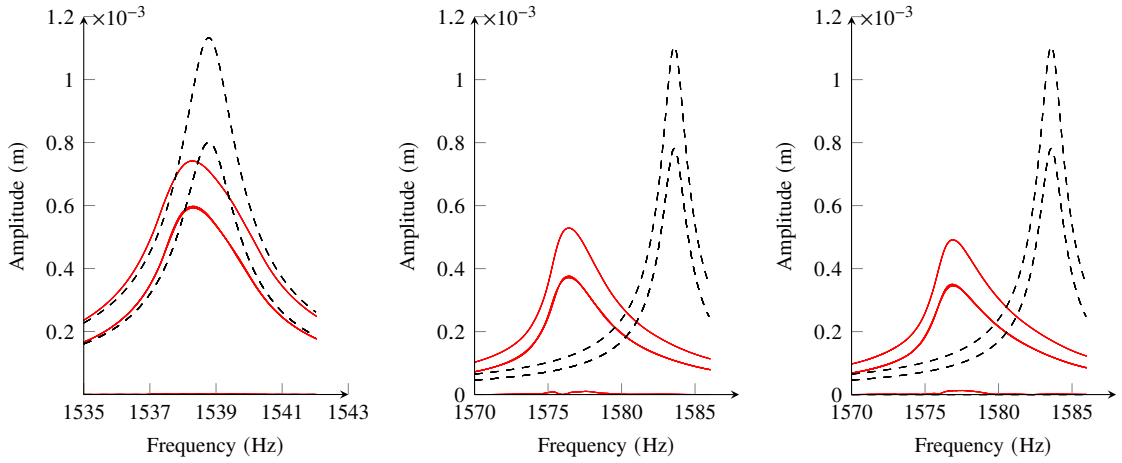

(a) Bladed disk. (b) Stuck bladed disk with dampers (c) Bladed disk with dampers.

Figure 13: Frequency forced response in the case of a standing wave excitation. (- -): linear solution (fully stuck); (—): Method 1.

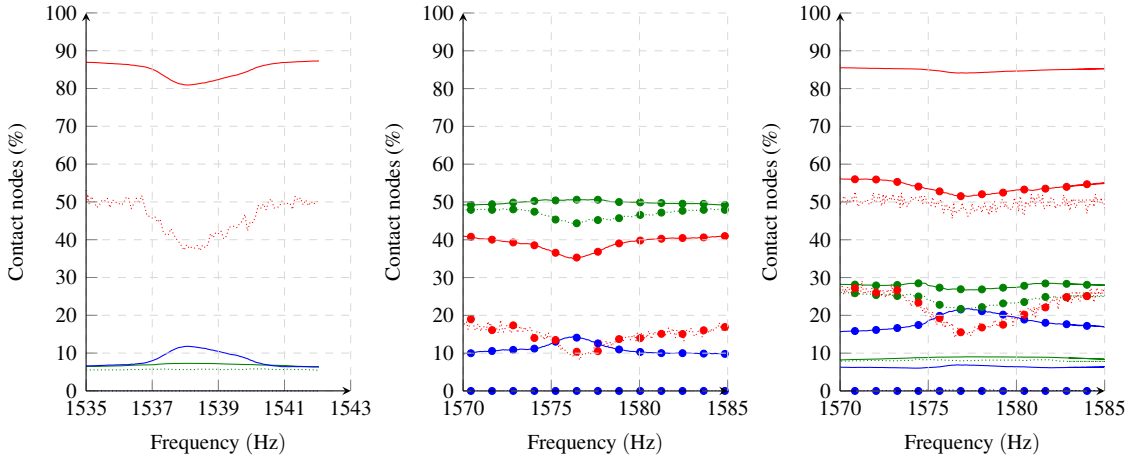

(a) Bladed disk. (b) Stuck bladed disk with dampers. (c) Bladed disk with dampers.

Figure 14: Average contact status of the nodes over a period, in the case of a standing wave excitation. The legend matches the one of Figure 12.

4.3. *Details of the spectral components of the responses of the three test cases under a standing wave excitation*

In this section, we highlight the spectral components of the frequency forced responses illustrated in Figure 13. These components are shown in Figure 15 for each test case.

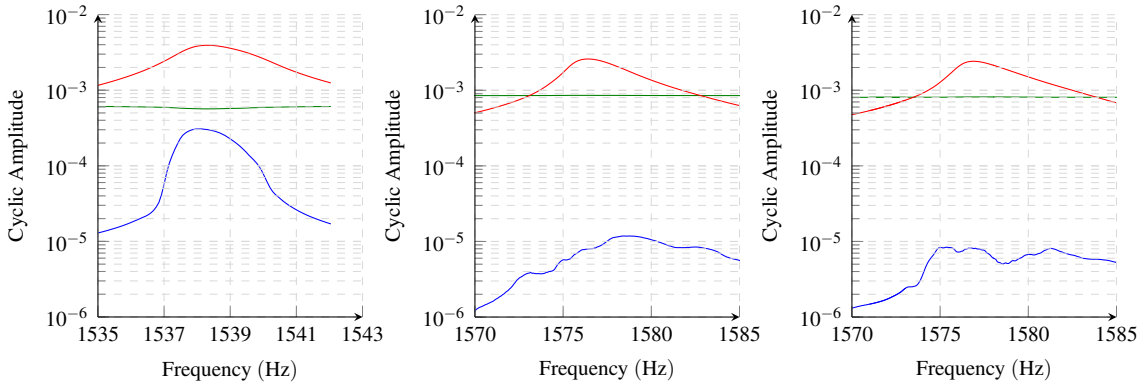

(a) Bladed disk. (b) Stuck bladed disk with dampers. (c) Bladed disk with dampers.

Figure 15: Spectral components of the responses shown in Figure 13 obtained with Method 1. (—): $\tilde{u}_0$, (—): $\tilde{u}_3$ and (—): $\tilde{u}_9$.

As can be seen in Figure 15, the response of the $0-$th nodal diameter shows only very slight variations over the frequency range studied here. The static preload controls the overall behavior and the small variations are due to nonlinear interactions. For the system with dampers (Figures 15b and 15c), the amplitude of $\tilde{u}_0$ is higher due to the additional centrifugal loading of the dampers.

For the bladed disk case, illustrated in Figure 15a, the ninth and third nodal diameters are coupled (the ratio between $\tilde{u}_9$ and $\tilde{u}_3$ is approximately 0.08). However, for the stuck bladed disk with dampers (Figure 15b), this ratio is only approximately 0.0046. Therefore, it appears from these results that the fir-tree attachment facilitates energy transfer between nodal diameters.

4.4. Influence of the friction coefficient

In this section, we study the impact of the friction coefficient on the nonlinear dynamics of the system. Three values of friction coefficient μ are studied: 0.15, 0.3 and 0.45. For brevity, only a traveling wave excitation was applied. The standing wave excitation gives analogous results. The simulations were performed with Method 2 only.

Figure 16 shows the influence of μ on the frequency response, focused around the first flexural mode for the three test cases. The results of Figure 16a are similar to those obtained in [1, 25]: as μ increases, the amplitude of vibration increases and moves closer to the stuck linear response.

Contrary to the bladed disk system case, the stuck bladed disk with dampers case and the full nonlinear system case do not give results close to the fully-stuck linear system (illustrated in the curved black dashed line see Figure 16) as μ increases. In fact, due to the static preload, some damper/blade interface nodes will always be separated no matter how high μ is. To illustrate this separation phenomenon, a vertical black dashed line is represented in Figures 16b and 16c. It represents the linear resonant frequency (located at 1576.6 Hz) of the system when all interface nodes that are not initially separated due to the static preload are imposed as being stuck. Naturally, the vibration of the system may change the contact status of these nodes to partial separation, and thus this vertical line does not represent the true asymptotic case.

For the $\mu = 0.15$ case, it was observed in Section 4.2.1 that the dampers governed most of the dynamics of the system. However, the blue and green lines in Figure 16c (corresponding to μ=0.3 and $\mu = 0.45$) show a different behavior from Figure 16b and thus present new dynamics of their own. To describe the system accurately, account must be taken of the entire structure and its inherent couplings occurring at the different interfaces.

Figure 17 illustrates the slipping state of the contact nodes for the three different values of μ and for the three test cases. For the stuck bladed disk with dampers (see Figure 16b),

as μ increases, the percentage of the slipping phase decreases from 30% to 15%. Less energy is thus dissipated and this may explain the amplitude increase as μ increases. The number of separated nodes (not represented here for brevity) is constant overall at approximately 50%. Figure 17c represents the slipping contact for the full system test case, we still observe a decrease in the percentage of the slipping phase when μ increases.

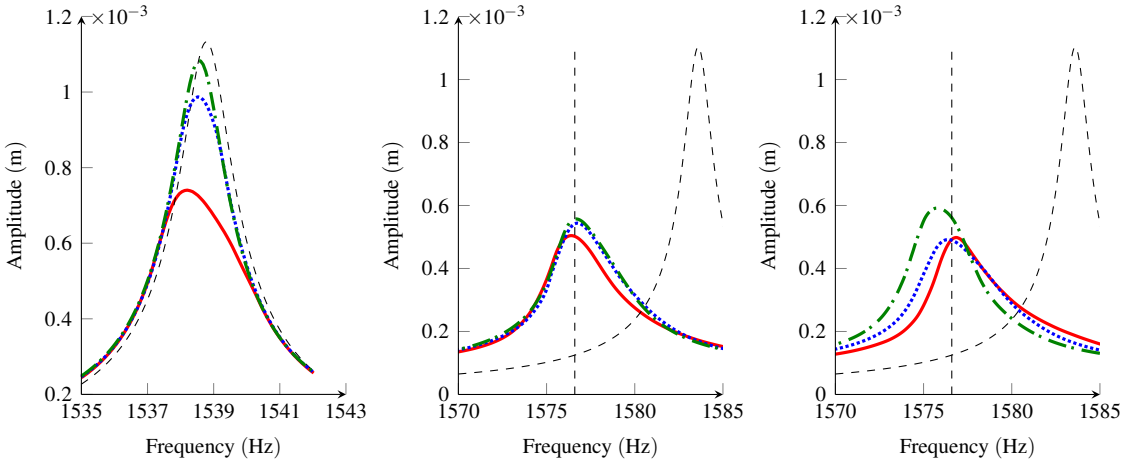

(a) Bladed disk. (b) Stuck bladed disk with dampers (c) Bladed disk with dampers.

Figure 16: Frequency forced responses for different values of friction coefficients. (——): $\mu = 0.15$; (·····): $\mu = 0.3$; (—·): $\mu = 0.45$, (- -): linear response (fully-stuck system). The vertical black dashed line indicates the linear frequency obtained with dampers nodes partially separated (the remaining are considered stuck).

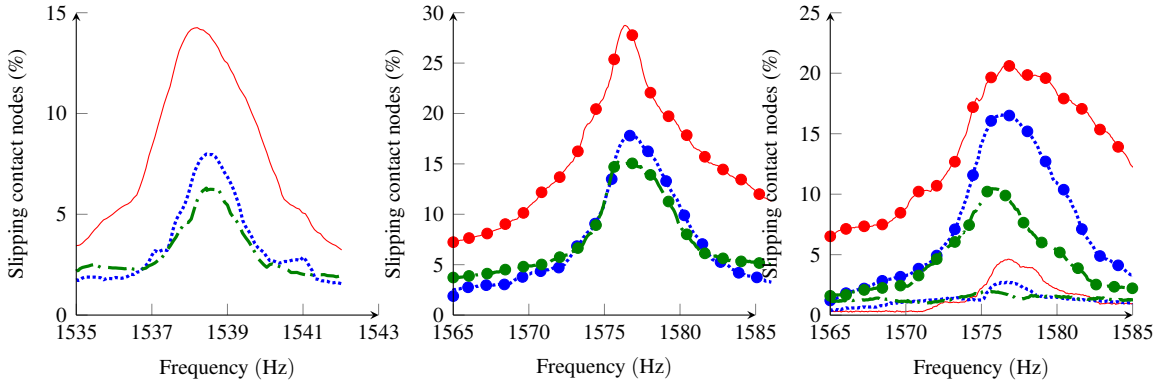

(a) Bladed disk. (b) Stuck bladed disk with dampers. (c) Bladed disk with dampers.

Figure 17: Average slipping contact status of the blades/disk interface nodes over a period for different friction coefficients. (—): $\mu = 0.15$; (·····): $\mu = 0.3$; (— · —): $\mu = 0.45$. The lines with (●) (and the same color code for different μ) represent the contact status of the damper/blade interface nodes.

4.5. Influence of the static preload

In this section, the friction coefficient was kept constant at $\mu = 0.15$ and three values of the rotational speed Ω were considered: $2200\,\mathrm{rad\,s^{-1}}$, $2500\,\mathrm{rad\,s^{-1}}$ and $2800\,\mathrm{rad\,s^{-1}}$. The variation of the centrifugal force will impact both the frictional nonlinear forces and the separation status. Frequency forced responses calculated with Method 2 were obtained for the three test cases and with the three aforementioned rotational speeds. These are illustrated in Figure 18. Figure 19 represents the slipping status of the nodes for the different static preloads and for each test case. To represent the slipping status of a test case for all rotational speeds, the frequencies of each simulation have been normalized by their respective resonant linear frequency.

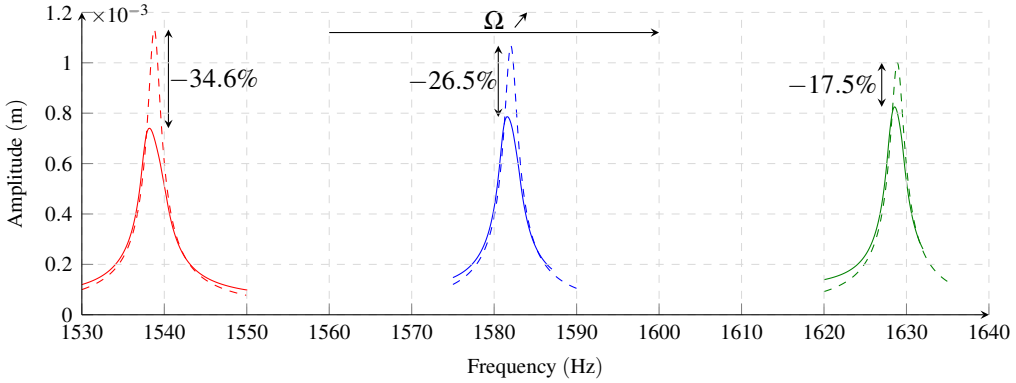

(a) Bladed disk.

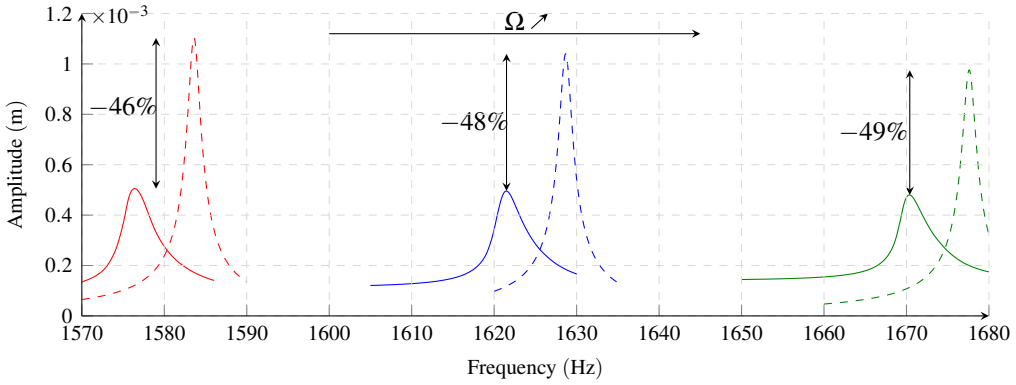

(b) Stuck bladed disk with dampers

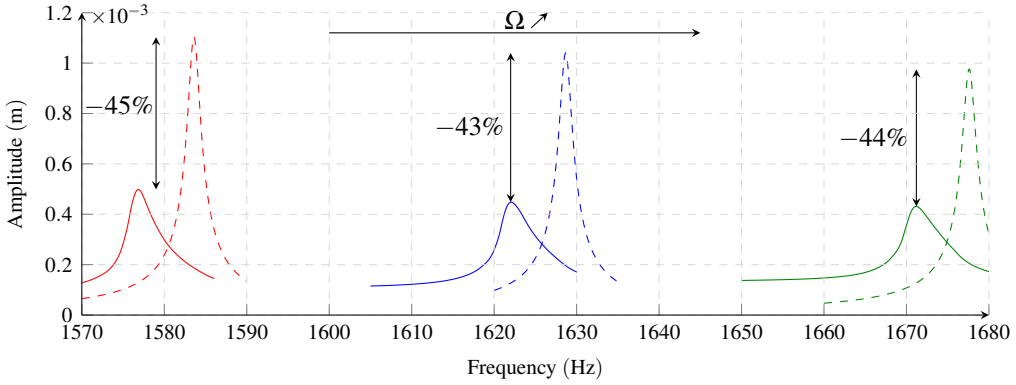

(c) Bladed disk with dampers.

Figure 18: Frequency forced responses for different values of rotational speeds. (—): $\Omega = 2200\,\mathrm{rad\,s^{-1}}$; (—): $\Omega = 2500\,\mathrm{rad\,s^{-1}}$; (—): $\Omega = 2800\,\mathrm{rad\,s^{-1}}$. (- -): linear responses (fully-stuck systems) with the same color code.

Figure 18 shows that, whatever the test case, the systems stiffens and the frequency of the first flexural mode increases when Ω increases. The relative amplitude difference at the resonant peaks between the linear and the associated nonlinear systems are given as a percentage in Figure 18. For the bladed disk test case (see Figure 18a), the greater the rotational speed, the less dissipation occurs, and thus the higher is the nonlinear amplitude. With high rotational speeds, the different solids composing the global structure are pressed against each other and are thus less likely to slip or get separated. This is confirmed by Figure 19a. For $\Omega = 2200\,\mathrm{rad\,s^{-1}}$, at the peak, almost 15% of the nodes are slipping, whereas this is approximately 10% for $\Omega = 2800\mathrm{rad\,s^{-1}}$.

The behavior of the stuck bladed disk with dampers is different: the dissipation increases slightly with the rotational speed (see Figure 18b). Nevertheless we still observe, in Figure 19b, that 30% of the nodes are slipping for $\Omega = 2200\,\mathrm{rad\,s^{-1}}$, but only 20% for $\Omega = 2800\,\mathrm{rad\,s^{-1}}$. Similarly to the bladed disk test case, higher loads lead to a greater number of nodes getting stuck. The increase in dissipation for the stuck bladed disk with dampers with Ω can be explained by higher normal load at the interfaces which leads to the tangential interface force also being higher. There is a compromise to be made in terms of dissipation: on one hand, less dissipation occurs when more nodes get stuck as Ω increases; on the other hand the normal load and thus the tangential force increase as Ω increases. For the stuck bladed disk, the latter effect is predominant, whereas for the bladed disk it is the former.

For the full nonlinear system, the dissipation varies very slightly and it seems that the two effects cancel each other out.

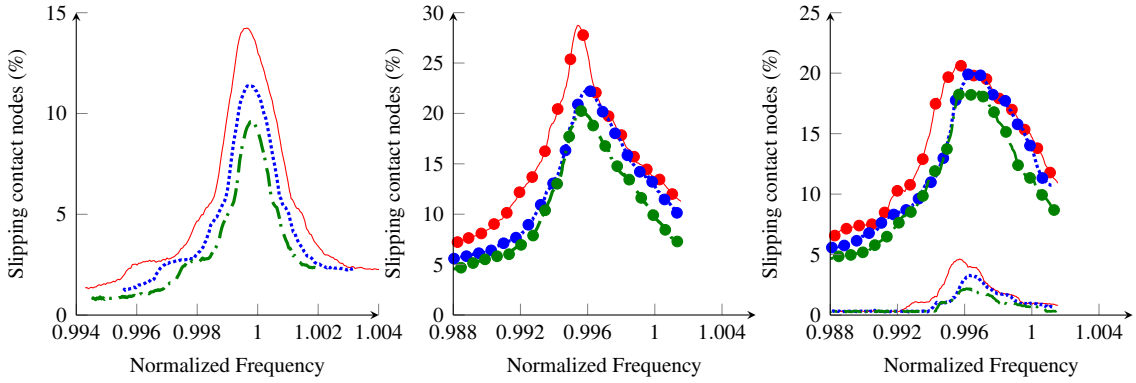

(a) Bladed disk. (b) Stuck bladed disk with dampers. (c) Bladed disk with dampers.

Figure 19: Average slipping status over a period. (—): $\Omega = 2200\,\mathrm{rad\,s^{-1}}$; (·····): $\Omega = 2500\,\mathrm{rad\,s^{-1}}$; (—·): $\Omega = 2800\,\mathrm{rad\,s^{-1}}$ for the blades/disk interface. The lines with (●) are associated with the damper/blades interface (same color code and line style).

5. Conclusion

The combination of recent reduction methodologies for cyclic symmetric systems and classical component mode synthesis were employed for the first time in realistic industrial finite-element models under static and dynamic loading. The cyclic strategies showed great accuracy, while reducing computation time significantly. Using these efficient reduction methods, the impact of dampers on a realistic compressor stage with a fir-tree attachment was studied. Different values of friction coefficients or centrifugal speed were used. The behavior of the full nonlinear system with frictional interfaces both at its root and with underplatfom dampers was shown to be highly complex and cannot simply be interpolated from either the damper nonlinear contact or the bladed disk contact.

These recent methods may lack representativeness for shrouded blades when shock dictates the dynamics of the system, as they are based on theoretical results obtained with friction nonlinearities only. Moreover, they are valid only for tuned structures. Nevertheless, in their framework of capabilities, these recent methodologies are particularly well

suited to assessing the performance of a new ROM procedure created to handle a wider range of systems, as was done with the CNCMS.

Acknowledgements

The authors would like to acknowledge the financial support of Safran Helicopter Engines. The authors acknowledge the help of Loïc Berthe for providing the finite-element models.

A. Dynamic Lagrangian Frequency Time method

In [26], a DLFT algorithm in velocity was employed. Such algorithm is efficient but does not converge when handling systems under static preload: the term $\mathbf{c}_0$ of the displacement (see Equation (13)) is removed from the algorithm due to the time derivative. Therefore, in this paper, a DLFT algorithm in position is used. A Schur condensation, as explained in [39], is applied on (14) and gives

$$\mathbf{Z}_r \mathbf{c}_r + \mathbf{c}_{\mathbf{f}_{\text{nl}}} = \mathbf{c}_{\mathbf{f}_{\text{r,ext}}}, \tag{A.1}$$

where $\mathbf{Z}_r$ is the relative dynamic stiffness matrix of the system, $\mathbf{c}_r$ denotes the relative harmonics components of the displacement, $\mathbf{c}_{\mathbf{f}_{\text{nl}}}$ corresponds to the harmonics of the nonlinear forces, and $\mathbf{c}_{\mathbf{f}_{\text{r,ext}}}$ contains the harmonics of the reduced external forces. The physical nonlinear forces are sought as

$$\mathbf{c}_{\mathbf{f}_{\text{nl}}} = \mathbf{c}_{\mathbf{f}_{\text{r,ext}}} - \mathbf{Z}_r \mathbf{c}_r + \varepsilon \left(\mathbf{c}_r - \mathbf{y}_r \right), \tag{A.2}$$

where ε is a penalty coefficient (the choice of this parameter is provided in [40]). $\mathbf{y}_r$ represents the harmonics of the relative displacement of the system's interface and must satisfy the contact/separation law as well as Coulomb's law. In the following, the algorithm is divided into two parts: the normal nonlinear forces and the tangential nonlinear forces.

A.1. Normal nonlinear forces

The normal nonlinear force (denoted by the subscript N) is separated into two parts: the optimized nonlinear forces (subscript u)

$$\mathbf{c}_{\mathbf{f}_{\mathrm{nl},N,u}} = \mathbf{c}_{\mathbf{f}_{\mathrm{r,ext,N}}} - \mathbf{Z}_{r,N}\mathbf{c}_r + \varepsilon \mathbf{c}_{r,N}, \tag{A.3}$$

and the correction of the nonlinear forces (subscript x) to satisfy the normal contact law (see Equation (17)):

$$\mathbf{c}_{\mathbf{f}_{\mathrm{nl}},N,x} = -\varepsilon \mathbf{y}_{r,N}. \tag{A.4}$$

A prediction of the nonlinear forces (subscript *pre*) is made by assuming that the solids are in contact,

$$\mathbf{c}_{\mathbf{f}_{\mathrm{nl},N,pre}} = \mathbf{c}_{\mathbf{f}_{\mathrm{nl},N,u}}. \tag{A.5}$$

Following the AFT procedure [15], this prediction is projected in the discretized time domain of length n_{it} ($t_n = \frac{nT}{n_{it}}$, with $n \in [\![1, n_{it}]\!]$ and T the time period of the solution) and gives $\mathbf{f}_{\mathrm{nl},N,pre}$. Two cases must be considered: if $\mathbf{f}_{\mathrm{nl},N,pre}(t_n) < 0$ (sticking case), then the prediction is correct (the solids are in contact), there is no correction and hence

$$\mathbf{f}_{\mathrm{nl},N,x}(t_n) = \mathbf{0} \tag{A.6}$$

otherwise if $\mathbf{f}_{\mathrm{nl},N,pre}(t_n) \geq 0$ (separation case), then the prediction is incorrect and must be corrected by

$$\mathbf{f}_{\mathrm{nl},N,x}(t_n) = \mathbf{f}_{\mathrm{nl},N,u}(t_n). \tag{A.7}$$

Finally the nonlinear forces are equal to

$$\mathbf{f}_{\mathrm{nl},N} = \mathbf{f}_{\mathrm{nl},N,u} - \mathbf{f}_{\mathrm{nl},N,x}. \tag{A.8}$$

The harmonic coefficients of $\mathbf{f}_{\mathrm{nl},N}$ are then obtained with the AFT procedure.

A.2. Tangential nonlinear forces

For the tangential force (denoted by subscript T), the nonlinear forces are also decomposed into an optimized part,

$$\mathbf{c}_{\mathbf{f}_{\mathrm{nl},T,u}} = \mathbf{c}_{\mathbf{f}_{\mathrm{r,ext,T}}} - \mathbf{Z}_{r,T}\mathbf{c}_r + \varepsilon \mathbf{c}_{r,T}, \tag{A.9}$$

and a correction part

$$\mathbf{c}_{\mathbf{f}_{\mathrm{nl},T,x}} = -\varepsilon \mathbf{y}_{r,T}. \tag{A.10}$$

Both of these terms are projected in the discretized time domain and gives $\left(\mathbf{f}_{\mathrm{nl},T,u}(t_n)\right)_{n\in[\![1,n_{it}]\!]}$ and $\left(\mathbf{f}_{\mathrm{nl},T,x}(t_n)\right)_{n\in[\![1,n_{it}]\!]}$. The prediction is equal to

$$\mathbf{f}_{\mathrm{nl},T,pre}(t_n) = \mathbf{f}_{\mathrm{nl},T,u}(t_n) - \mathbf{f}_{\mathrm{nl},T,x}(t_{n-1}). \tag{A.11}$$

Initially, the solids are supposed to be stuck ($\mathbf{f}_{\mathrm{nl},T,x}(t_0) = \mathbf{0}$). For each discretized time $(t_n)_{n\in[\![1,n_{it}]\!]}$, the tangential forces are evaluated. If, at t_n the solids are separated then there is no tangential forces which implies

$$\mathbf{f}_{\mathrm{nl},T,x}(t_n) = \mathbf{f}_{\mathrm{nl},T,u}(t_n) \tag{A.12}$$

If, at t_n, the solids are in contact then two cases must be distinguished: if $\|\mathbf{f}_{\mathrm{nl},T,pre}(t_n)\| < \mu\left|\mathbf{f}_{\mathrm{nl},N}\right|$ then the solids are stuck are the prediction was correct:

$$\mathbf{f}_{\mathrm{nl},T,x}(t_n) = \mathbf{f}_{\mathrm{nl},T,x}(t_{n-1}). \tag{A.13}$$

Otherwise $\|\mathbf{f}_{\mathrm{nl},T,pre}(t_n)\| \geq \mu\left|\mathbf{f}_{\mathrm{nl},N}\right|$ then the solids are slipping and the correction is equal to

$$\mathbf{f}_{\mathrm{nl},T,x}(t_n) = \mathbf{f}_{\mathrm{nl},T,x}(t_{n-1}) + \mathbf{f}_{\mathrm{nl},T,pre}(t_n)\left(1 - \frac{\mu\left|\mathbf{f}_{\mathrm{nl},N}(t_n)\right|}{\|\mathbf{f}_{\mathrm{nl},T,pre}(t_n)\|}\right) \tag{A.14}$$

Finally the nonlinear forces are equal to

$$\mathbf{f}_{\mathrm{nl},T} = \mathbf{f}_{\mathrm{nl},T,u} - \mathbf{f}_{\mathrm{nl},T,x}. \tag{A.15}$$

To free ourself from the initial assumption ($\mathbf{f}_{\mathrm{nl},T,x}(t_0) = \mathbf{0}$), the computation of the tangential nonlinear forces is done for two periods of time.

References

[1] E. P. Petrov, D. J. Ewins, Advanced Modeling of Underplatform Friction Dampers for Analysis of Bladed Disk Vibration, Journal of Turbomachinery 129 (1) (2007) 143–150. doi:10.1115/1.2372775.

[2] E. P. Petrov, Explicit Finite Element Models of Friction Dampers in Forced Response Analysis of Bladed Disks, Journal of Engineering for Gas Turbines and Power 130 (2), publisher: American Society of Mechanical Engineers Digital Collection (Mar. 2008). doi:10.1115/1.2772633.

[3] M. M. Gola, C. Gastaldi, Understanding Complexities in Underplatform Damper Mechanics (2014) V07AT34A002doi:10.1115/GT2014-25240.

[4] B. D. Yang, C. H. Menq, Characterization of Contact Kinematics and Application to the Design of Wedge Dampers in Turbomachinery Blading: Part 1—Stick-Slip Contact Kinematics, Journal of Engineering for Gas Turbines and Power 120 (2) (1998) 410–417, publisher: American Society of Mechanical Engineers Digital Collection. doi:10.1115/1.2818138.

[5] K. Y. Sanliturk, D. J. Ewins, A. B. Stanbridge, Underplatform Dampers for Turbine Blades: Theoretical Modeling, Analysis, and Comparison With Experimental Data, Journal of Engineering for Gas Turbines and Power 123 (4) (1998) 919–929. doi:10.1115/1.1385830.

[6] L. Pesaresi, L. Salles, A. Jones, J. S. Green, C. W. Schwingshackl, Modelling the nonlinear behaviour of an underplatform damper test rig for turbine applications, Mechanical Systems and Signal Processing 85 (2017) 662–679. doi:10.1016/j.ymssp.2016.09.007.

[7] L. Pesaresi, J. Armand, C. W. Schwingshackl, L. Salles, C. Wong, An advanced underplatform damper modelling approach based on a microslip contact model, Journal of Sound and Vibration 436 (2018) 327–340. doi:10.1016/j.jsv.2018.08.014.

[8] C. W. Schwingshackl, E. P. Petrov, D. J. Ewins, Effects of Contact Interface Parameters on Vibration of Turbine Bladed Disks With Underplatform Dampers, Journal of Engineering for Gas Turbines and Power 134 (3), publisher: American Society of Mechanical Engineers Digital Collection (Mar. 2012). doi:10.1115/1.4004721.

[9] B. He, H. Ouyang, X. Ren, S. He, Dynamic Response of a Simplified Turbine Blade Model with Under-Platform Dry Friction Dampers Considering Normal Load Variation, Applied Sciences 7 (3) (2017) 228. doi:10.3390/app7030228.

[10] C. M. Firrone, S. Zucca, M. M. Gola, The effect of underplatform dampers on the forced response of bladed disks by a coupled static/dynamic harmonic balance method, International Journal of Non-Linear Mechanics 46 (2) (2011) 363–375. doi:10.1016/j.ijnonlinmec.2010.10.001.

[11] S. Zucca, C. M. Firrone, Nonlinear dynamics of mechanical systems with friction contacts: Coupled static and dynamic Multi-Harmonic Balance Method and multiple solutions, Journal of Sound and Vibration 333 (3) (2014) 916–926. doi:10.1016/j.jsv.2013.09.032.

[12] C. M. Firrone, S. Zucca, Modelling Friction Contacts in Structural Dynamics and its Application to Turbine Bladed Disks, Numerical Analysis - Theory and Application (Sep. 2011). doi:10.5772/25128.

[13] S. Nacivet, C. Pierre, F. Thouverez, L. Jézéquel, A dynamic Lagrangian frequency–time method for the vibration of dry-friction-damped systems, Journal of

Sound and Vibration 265 (1) (2003) 201–219. doi:10.1016/S0022-460X(02)01447-5.

[14] G. Kerschen, M. Peeters, J. C. Golinval, A. F. Vakakis, Nonlinear normal modes, Part I: A useful framework for the structural dynamicist, Mechanical Systems and Signal Processing 23 (1) (2009) 170–194. doi:10.1016/j.ymssp.2008.04.002.

[15] T. M. Cameron, J. H. Griffin, An Alternating Frequency/Time Domain Method for Calculating the Steady-State Response of Nonlinear Dynamic Systems, Journal of Applied Mechanics 56 (1) (1989) 149–154. doi:10.1115/1.3176036.

[16] M. Mitra, S. Zucca, B. I. Epureanu, Adaptive Microslip Projection for Reduction of Frictional and Contact Nonlinearities in Shrouded Blisks, Journal of Computational and Nonlinear Dynamics 11 (4) (2016) 041016. doi:10.1115/1.4033003.

[17] D.-M. Tran, Component mode synthesis methods using partial interface modes: Application to tuned and mistuned structures with cyclic symmetry, Computers & Structures 87 (17) (2009) 1141–1153. doi:10.1016/j.compstruc.2009.04.009.

[18] E. P. Petrov, A High-Accuracy Model Reduction for Analysis of Nonlinear Vibrations in Structures With Contact Interfaces, Journal of Engineering for Gas Turbines and Power 133 (10), publisher: American Society of Mechanical Engineers Digital Collection (Oct. 2011). doi:10.1115/1.4002810.

[19] F. Mashayekhi, A. S. Nobari, S. Zucca, Hybrid reduction of mistuned bladed disks for nonlinear forced response analysis with dry friction, International Journal of Non-Linear Mechanics 116 (2019) 73–84. doi:10.1016/j.ijnonlinmec.2019.06.001.

[20] S. Mehrdad Pourkiaee, S. Zucca, A Reduced Order Model for Nonlinear Dynamics of Mistuned Bladed Disks With Shroud Friction Contacts, Journal of Engineering for Gas Turbines and Power 141 (1), publisher: American Society of Mechanical Engineers Digital Collection (Jan. 2019). doi:10.1115/1.4041653.

[21] R. H. MacNeal, NASTRAN cyclic symmetry capability. [application to solid rocket propellant grains and space antennas], 1973.

[22] D. L. Thomas, Dynamics of rotationally periodic structures, International Journal for Numerical Methods in Engineering 14 (1) (1979) 81–102. doi:10.1002/nme.1620140107.

[23] F. Georgiades, M. Peeters, G. Kerschen, J. C. Golinval, M. Ruzzene, Modal Analysis of a Nonlinear Periodic Structure with Cyclic Symmetry, AIAA Journal 47 (4) (2009) 1014–1025. doi:10.2514/1.40461.

[24] E. P. Petrov, A Method for Use of Cyclic Symmetry Properties in Analysis of Nonlinear Multiharmonic Vibrations of Bladed Disks, Journal of Turbomachinery 126 (1) (2004) 175. doi:10.1115/1.1644558.

[25] E. Lemoine, D. Nélias, F. Thouverez, C. Vincent, Influence of fretting wear on bladed disks dynamic analysis, Tribology International 145 (2020) 106148. doi:10.1016/j.triboint.2019.106148.

[26] S. Quaegebeur, B. Chouvion, F. Thouverez, Model reduction of nonlinear cyclic structures based on their cyclic symmetric properties, Mechanical Systems and Signal Processing 145 (2020) 106970. doi:10.1016/j.ymssp.2020.106970.

[27] C. Joannin, B. Chouvion, F. Thouverez, J.-P. Ousty, M. Mbaye, A nonlinear component mode synthesis method for the computation of steady-state vibrations in non-

765 conservative systems, Mechanical Systems and Signal Processing 83 (2017) 75–92.
766 doi:10.1016/j.ymssp.2016.05.044.

767 [28] C. Joannin, F. Thouverez, B. Chouvion, Reduced-order modelling using nonlinear
768 modes and triple nonlinear modal synthesis, Computers & Structures 203 (2018) 18–
769 33. doi:10.1016/j.compstruc.2018.05.005.

770 [29] R. R. Craig, M. C. C. Bampton, Coupling of substructures for dynamic analyses.,
771 AIAA Journal 6 (7) (1968) 1313–1319. doi:10.2514/3.4741.

772 [30] B. D. Yang, M. L. Chu, C. H. Menq, Stick–slip–sepratation analysis and non-linear
773 stiffness and damping characterization of friction contacts having variable normal
774 load, Journal of Sound and Vibration 210 (4) (1998) 461–481. doi:10.1006/jsvi.
775 1997.1305.

776 [31] D. Laxalde, F. Thouverez, Complex non-linear modal analysis for mechanical sys-
777 tems: Application to turbomachinery bladings with friction interfaces, Journal of
778 Sound and Vibration 322 (4) (2009) 1009–1025. doi:10.1016/j.jsv.2008.11.
779 044.

780 [32] M. Krack, L. Panning-von Scheidt, J. Wallaschek, A method for nonlinear modal
781 analysis and synthesis: Application to harmonically forced and self-excited me-
782 chanical systems, Journal of Sound and Vibration 332 (25) (2013) 6798–6814.
783 doi:10.1016/j.jsv.2013.08.009.

784 [33] R. Valid, R. Ohayon, Théorie et calcul statique et dynamique des structures à
785 symétries cycliques, La Recherche aérospatiale (1985) 251–263.

786 [34] M. Mitra, B. I. Epureanu, Dynamic Modeling and Projection-Based Reduction Meth-
787 ods for Bladed Disks With Nonlinear Frictional and Intermittent Contact Interfaces,

Applied Mechanics Reviews 71 (5), publisher: American Society of Mechanical Engineers Digital Collection (Sep. 2019). doi:10.1115/1.4043083.

[35] B. Cochelin, N. Damil, M. Potier-Ferry, Méthode asymptotique numérique, Methodes numériques, Hermes Lavoissier, 2007.

[36] M. Peeters, R. Viguié, G. Sérandour, G. Kerschen, J. C. Golinval, Nonlinear normal modes, Part II: Toward a practical computation using numerical continuation techniques, Mechanical Systems and Signal Processing 23 (1) (2009) 195–216. doi:10.1016/j.ymssp.2008.04.003.

[37] G. Kerschen, M. Peeters, J. Golinval, A. Vakakis, Nonlinear normal modes, part i: A useful framework for the structural dynamicist, Mechanical Systems and Signal Processing 23 (1) (2009) 170 – 194, special Issue: Non-linear Structural Dynamics. doi:https://doi.org/10.1016/j.ymssp.2008.04.002.

[38] M. Krack, J. Gross, Theory of harmonic balance, in: Harmonic Balance for Nonlinear Vibration Problems, Mathematical Engineering, Springer International Publishing, Cham, 2019, pp. 11–46. doi:10.1007/978-3-030-14023-6_2.

[39] O. Poudou, C. Pierre, Hybrid Frequency-Time Domain Methods for the Analysis of Complex Structural Systems with Dry Friction Damping, in: 44th AIAA/ASME/ASCE/AHS/ASC Structures, Structural Dynamics, and Materials Conference, American Institute of Aeronautics and Astronautics. doi:10.2514/6.2003-1411.

[40] D. Charleux, Etude des effets de la friction en pied d'aube sur la dynamique des roues aubagées, phdthesis, Ecole Centrale de Lyon (Mar. 2006).